Measuring Nonlocal Brane Order with Error-Corrected Quantum Gas Microscopes

Junhyeok Hur,[1,*] Wonjun Lee,[2,3,*] Kiryang Kwon,[1] SeungJung Huh,[1] Gil Young Cho,[2,3,4,†] and Jae-yoon Choi[1,‡]

[1]*Department of Physics, Korea Advanced Institute of Science and Technology, Daejeon 34141, Republic of Korea*

[2]*Department of Physics, Pohang University of Science and Technology, Pohang, 37673, Republic of Korea*

[3]*Center for Artificial Low Dimensional Electronic Systems, Institute for Basic Science, Pohang 37673, Republic of Korea*

[4]*Asia-Pacific Center for Theoretical Physics, Pohang, 37673, Republic of Korea*

(Received 16 May 2023; accepted 15 November 2023; published 8 January 2024)

Exotic quantum many-body states, such as Haldane and spin liquid phases, can exhibit remarkable features like fractional excitations and non-Abelian statistics and offer new understandings of quantum entanglement in many-body quantum systems. These phases are classified by nonlocal correlators that can be directly measured in atomic analog quantum simulating platforms, such as optical lattices and Rydberg atom arrays. However, characterizing these phases in large systems is experimentally challenging because they are sensitive to local errors like atom loss, which suppress its signals exponentially. Additionally, protocols for systematically identifying and mitigating uncorrelated errors in analog quantum simulators are lacking. Here, we address these challenges by developing an error-correction method for large-scale neutral atom quantum simulators using optical lattices. Our error-correction method can distinguish correlated particle-hole pairs from uncorrelated holes in the Mott insulator. After removing the uncorrelated errors, we observe a dramatic improvement in the nonlocal parity correlator and find the perimeter scaling law. Furthermore, the error model provides a statistical estimation of fluctuations in site occupation, from which we measure the generalized brane correlator and confirm that it can be an order parameter for Mott insulators in two dimensions. Our work provides a promising avenue for investigating and characterizing exotic phases of matters in large-scale quantum simulators.

DOI: 10.1103/PhysRevX.14.011003

Subject Areas: Atomic and Molecular Physics, Quantum Physics

I. INTRODUCTION

Conventional phases of matter can be characterized by measuring local order parameters, which represent the degree of symmetry breaking. However, it has become clear that the concept of "nonlocal order parameters" (NLOs) is crucial to distinguish different types of exotic quantum orders [1–5]. The Haldane chain [6] is a paradigmatic example, where a string-type nonlocal correlator [2] can reveal the hidden quantum phase. Because of the direct accessibility of atomic distribution with a single-site resolution [7,8], ultracold atoms in optical lattices have provided an unprecedented opportunity to study NLOs. For example, the unity filling Mott insulating (MI) phase has been a test bed for studying NLOs [9,10] because the phase hosts bounded particle-hole pairs as virtual excitations on top of the constant density distribution due to a finite tunneling strength. The string correlator has been measured in a one-dimensional Mott insulating phase [11], and recent experiments using Fermi gases have applied the string-type correlator to reveal hidden antiferromagnetic correlations in doped Fermi-Hubbard chains [12] and to probe the Haldane phase in Fermi-Hubbard ladder [13]. Efforts have been made to extend the NLO to higher dimensions, with the recent suggestion of generalized brane correlators in two-dimensional Hubbard models [14,15]. Moreover, Wilson loops have been exploited to probe the topological $\mathbb{Z}_2$ spin liquid phase in Rydberg atom arrays [16,17].

However, these nonlocal correlators can be easily destroyed by experimental imperfections, such as detection atom loss, limiting its practical usage. When measuring the brane parity correlator for N sites, as an example, each site may experience a small loss (error) rate $\eta \ll 1$ during imaging process. The atom loss can occur in all lattice sites independently, so this can exponentially suppress the fidelity $\mathcal{F}$ of the N-site parity measurements

*These authors contributed equally to this work.

†gilyoungcho@postech.ac.kr

‡jaeyoon.choi@kaist.ac.kr

$\mathcal{F} \sim (1-\eta)^N$. Hence, to reliably evaluate the NLO in a large-scale quantum simulator, it is essential to alleviate the effect of the incoherent error as much as possible. In literature, the systematic method to identify and reduce the effect of various types of errors from the measurement data is collectively called the error mitigation protocol [18]. Unfortunately, there has been little progress [19,20] on such protocols in ultracold atom simulators.

Here, we present a new error-correction (EC) method for atomic quantum simulator and demonstrate its efficacy by measuring nonlocal order parameters in the two-dimensional Bose-Hubbard (BH) model. The EC method is based on mapping the parity snapshot data of the Bose-Hubbard system to the spin configurations of a 2D Ising error model, enabling the identification of the correlated particle-hole pairs and remove uncorrelated holes from the snapshot. The brane parity correlators with error-corrected snapshots then can successfully distinguish the Mott insulator and superfluid phases in a large-scale system containing more than 100 lattice sites. We further find that the brane parity correlator satisfies the expected perimeter scaling laws. Moreover, we are able to infer the fluctuations in the site occupation number in the MI because the EC method can assign the particle-hole pairs from the parity snapshots. This enables us to evaluate the generalized brane correlator and confirm recent predictions that it can serve as an order parameter for the two-dimensional Mott insulators [15].

II. BOSE-HUBBARD MODEL

As an experimental platform, we employ ultracold ^{7}Li atoms in a square optical lattice [Fig. 1(a)] to realize a two-dimensional BH model [21,22]:

$$H = -J\sum_{\langle i,j\rangle}(b_i^\dagger b_j + \text{H.c.}) + \frac{U}{2}\sum_i n_i(n_i-1) + \sum_i \varepsilon_i n_i. \quad (1)$$

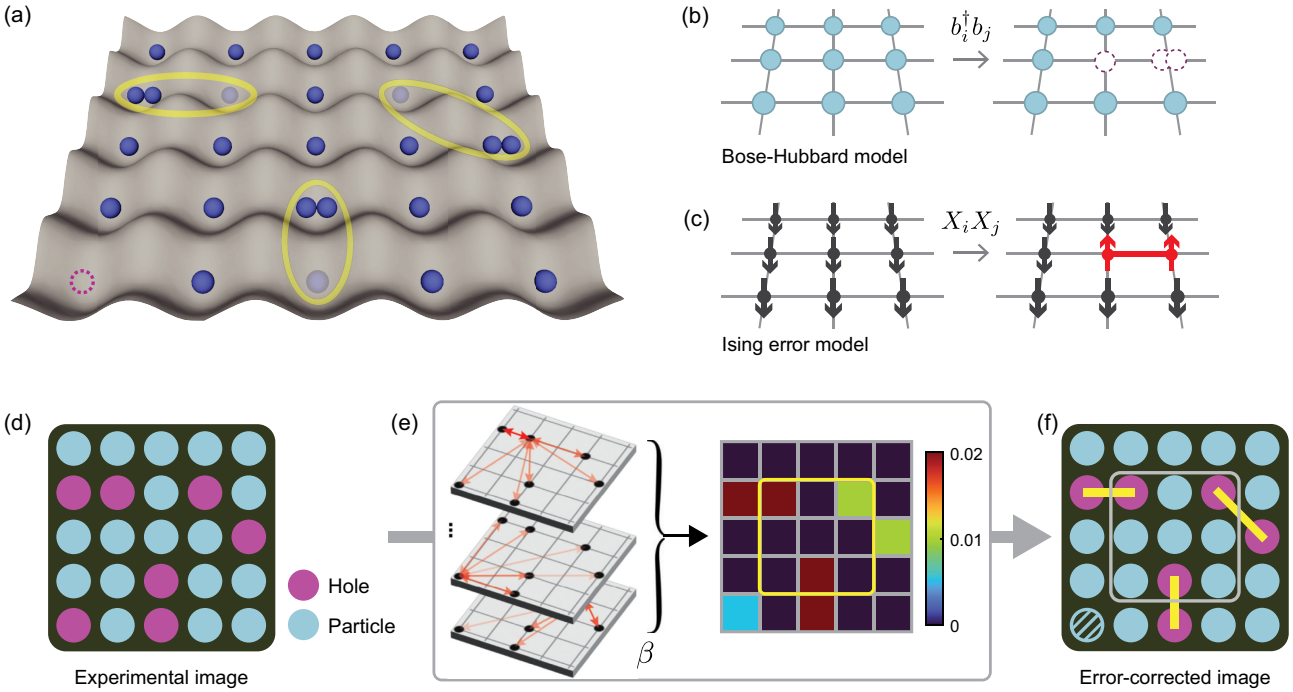

FIG. 1. Schematic diagram of the error-correction protocol. (a) Mott insulating (MI) phase of neutral atoms in a two-dimensional square optical lattice. The entangled particle-hole pairs (yellow circles) can be generated because of the finite tunneling amplitude. An uncorrelated hole (purple dashed circle) can be found in the MI phase because of experimental imperfections. (b),(c) Correspondence between the Ising error model and the Bose-Hubbard (BH) model. In the BH model, the particle-hole excitations can be created by the tunneling operator $b_i^\dagger b_j$ on the background of a unity filling. After the fluorescence imaging, atoms in the doubly occupied sites are lost, resulting in an empty lattice site (dashed circles). These sites have the same even parity. In the Ising model, the Pauli-X correlator $X_i X_j$ creates a paired spin-up excitation along a link (red line). The particle-hole pairs after the parity projection can be considered as the excitations in the Ising model. (d) Experimental snapshot image of MI phase. The correlated particle-hole pairs are not distinguishable from the uncorrelated hole. (e) The error identification protocol. For a given single experimental image, we evaluate the probability $p(i_E \leftrightarrow j_E)$ for the pairs of the parity flips at the sites i_E and j_E. The pairs with higher (lower) probabilities are marked by dark (light) red arrows. The uncorrelated hole at the site i_E can be identified when the probabilities for all possible pairs $p(i_E \leftrightarrow j_E)$ is smaller than the (pair of) error rate η^2. (f) Error-corrected image. Correlated particle-hole pairs (tied with yellow lines) and the uncorrelated hole (blue shaded circle) are identified. To determine the fitting parameter β of the error model, we compare the brane correlator in the BH model (gray box) and the domain wall operator in the Ising model (yellow box); see Appendix C 5.

The bosonic creation (annihilation) operator at lattice site i is $b_i^\dagger$ (b_i), $n_i = b_i^\dagger b_i$ is the site occupation number, J is the tunneling strength, U is the on-site interaction energy, and ε_i is the energy offset from harmonic confinement in the lattice beam. Moreover, we employ a high-resolution fluorescence imaging system [23] and detect the number parity $P_i = (-1)^{n_i}$ at lattice site i. Notably, we can prepare a large-sized unity filling Mott insulator (40 sites diameter with more than 1000 atoms) by tuning the scattering length of the atoms using a Feshbach resonance. In this study, we focus on the central area of the $\mathcal{D}_c = 20 \times 20$ lattice sites to minimize trap inhomogeneity. For the brane correlators, we take all the possible $L \times L$ domains within $\mathcal{D}_c$ (Appendix A).

However, the detection of the parity and preparation of MI states are not perfect because of the various errors, such as particle loss during the imaging process or free holes generated from the thermal fluctuations. Here, we attempt to simulate the ground state of MI; the finite temperature is also the source of errors. We will collectively call these holes "uncorrelated errors" because the Mott insulator is well below the melting temperature [8,24] so that they occur independently at each site. It contrasts with the correlated parity flips due to the virtual particle-hole excitations over the MI. We estimate the rate η of such uncorrelated errors to be ~3% (Appendix A). Despite being small, this can dramatically diminish the ability to measure multipoint correlators in MI including the brane parity correlator $\langle \mathcal{O}_\mathcal{D} \rangle = \langle \prod_{i \in D} P_i \rangle$, where $\langle \cdots \rangle$ refers to ensemble average. For example, see Fig. 2(b) for $\langle \mathcal{O}_\mathcal{D} \rangle$ with $\mathcal{D} = 12 \times 12$, where the bare experimental data (open circle) do not show any noticeable feature, regardless of the various lattice depths or tunneling energy. We can barely observe the brane parity correlator signal only for a small system size with $L = 6$ [Fig. 2(b) inset, open circle]. Hence, it is imperative to remove the effect of the uncorrelated local errors in experiments to observe the nonlocal correlators in noisy environments.

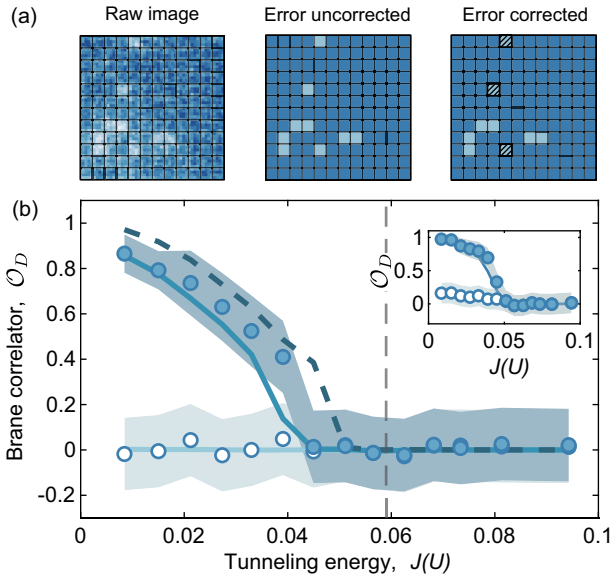

FIG. 2. Brane parity correlator. (a) The error-corrected image in the experiment. The error-correction method detects and removes the uncorrelated holes in the snapshots. (b) Brane parity correlator in two-dimensional Bose-Hubbard model with the domain size $\mathcal{D} = 12 \times 12$. Without the EC (open circle), the brane correlator hardly distinguishes MI and the superfluid phase. The EC-assisted measurement (closed circle) shows a dramatic signal increase and can identify the superfluid-to-Mott-insulating phase transition. Inset shows the brane parity correlator with $L = 6$. Solid lines are the QMC simulation (Appendix B) at $T = 0.083U$ and uncorrelated hole rate $\eta = 0.0277$ with EC (blue) and without (light blue) the EC method. The experimental data agree well with the QMC simulation. They can compare with the QMC simulation with no uncorrelated error $\eta = 0$ at the zero temperature $T = 0$ (dark blue dotted line). The zero-temperature data are obtained by the extrapolation of the finite temperature data (Fig. 7). The gray dotted line represents the quantum critical point in 2D, estimated by the QMC simulation $(J/U)_c = 0.059$ [25]. Each data point is obtained over 40 independent experimental runs, and the shaded region denotes the maximum standard error (Appendix A).

III. ERROR-CORRECTION METHOD

Our EC method is designed to circumvent the difficulty efficiently and allow the calculation of nonlocal brane correlators [14,15], which can accurately distinguish the two phases of the BH model. It is based on mapping the parity snapshots of the BH model to the spin configurations of the 2D Ising error model:

$$|\psi(\beta)\rangle = \frac{e^{\beta \sum_{\langle i,j \rangle} X_i X_j}}{\sqrt{\mathcal{Z}}} \prod_{\forall k} |0\rangle_k. \tag{2}$$

We map a bit $\sigma = 0, 1$, which parametrizes the number parity $P = (-1)^{\sigma+1}$ of the BH model, to the spin Z in the Ising model; i.e., $Z_i|0\rangle_i = |0\rangle_i$ and $Z_i|1\rangle_i = -|1\rangle_i$. Here, $\langle i, j \rangle$ is a link in a 2D square lattice and X_i is the Pauli-X operator, which flips the parity; e.g., $X_i|0\rangle = |1\rangle$. $\mathcal{Z}$ is a normalization factor, and β is a single fitting parameter in our EC. The properties of $|\Psi(\beta)\rangle$, including the phases and phase transition, have been well investigated in the literature [26]. For example, $|\Psi(\beta)\rangle$ is known to be in the paramagnet phase for $\beta < \beta_c \approx 0.22$, and in the ferromagnetic phase (spins are aligned along the X direction) for $\beta > \beta_c$.

Our key observation is that $|\Psi(\beta)\rangle$ at small $\beta < \beta_c$ can be naturally identified with the parity snapshots of MI. For example, $|\Psi(\beta \to 0)\rangle$ represents the uniform parity configuration. It naturally corresponds to the MI with homogeneous site occupation, where the boson tunneling strength J/U is strongly suppressed. When J/U is finite but small, there are exponentially short-ranged, virtual particle-hole excitations above the uniform background

[Fig. 1(b)]. They will appear as a pair of bit flips in the snapshots. Such virtual excitations can be well captured by a nonzero but small β in Eq. (2),

$$|\Psi(\beta)\rangle \approx \left(1+\beta\sum_{\langle i,j\rangle} X_i X_j + O(\beta^2)\right)\prod_{k\in\mathcal{D}}|0\rangle_k,$$

which allow the pair of parity flips above the uniform spin configuration [Fig. 1(c)]. The higher-order terms in β capture the longer-distance pair excitations, which are however exponentially short-ranged in the paramagnetic phase. Intuitively, β controls the strength of the virtual particle-hole fluctuations, which approaches β_c as J/U approaches the transition toward superfluid (SF). In practice, β can be efficiently calibrated for the given experimental snapshot data (Appendix C 5).

The error model allows us to extract the desired information hidden in the snapshot data. In particular, it can reveal the origin of the parity flips. The important quantity in this task is the spin-spin correlator,

$$p(i_E \leftrightarrow j_E) \approx \frac{1}{4}\langle X_{i_E} X_{j_E}\rangle^2, \tag{3}$$

which approximates the probability for the two parity flips at the sites i_E and j_E to appear from the virtual particle-hole fluctuation. Intuitively, the virtual particle-hole pairs in the BH model [Fig. 1(b)] correspond to XX operators [Fig. 1(c)] in the Ising model, and thus $p(i_E \leftrightarrow j_E)$ is naturally related to the spin-spin correlator. A more rigorous statement can be found in the Appendix C 2.

This provides a systematic route to identify the uncorrelated holes for a given experimental snapshot. The most straightforward yet quite effective strategy is to perform the maximum likelihood test between the two scenarios for each pair of parity flips to occur. Specifically, for each snapshot [Fig. 1(d)], we first calculate the probability $p(i_E \leftrightarrow j_E)$ for all the possible pairs of the parity flips [Fig. 1(e)]. We then pair each parity flip at i_E with another at j_E, which generates the maximum $p(i_E \leftrightarrow j_E)$ among many others [Fig. 1(e)]. When a parity flip at i_E satisfies

$$\max_{\forall\ j_E\neq i_E} p(i_E \leftrightarrow j_E) < \eta^2,$$

with the uncorrelated error rate η, then we conclude that the error is not correlated with all the other parity flips. Hence, it must be uncorrelated local errors, and we correct such errors from the snapshot data [Fig. 1(f)] achieving our goal.

To demonstrate the effectiveness of our error-correction protocol in removing uncorrelated errors, we utilize numerical images generated from stochastic series expansion quantum Monte Carlo (QMC) simulation [27,28] After preparing a numerical image, we add random holes with its population rate η and compare the error-corrected images with the original image. In the Mott insulator phase, we observe a negligible difference between the two images (Fig. 8).

It is worth noting that all the calculations and data processing involved in our EC procedure can be carried out very efficiently on a classical computer. It is more efficient than the classical simulation of the BH model, such as QMC simulation of the ground state. Additionally, even if one has a method that exactly simulates the ground state, it is not *a priori* clear how to identify the local errors in experimental parity snapshots. Only when one has a proper error model for the system, the pairing of the parity flips and identification of the incoherent local errors can be correctly done.

A few minor remarks are in order. First, the input data of our EC protocol, such as η, can be obtained within the experiments. For instance, running the EC protocol does not involve any extra QMC simulation of the BH model. Second, it should also be remarked that our work does not pursue achieving the quantum error correction (QEC) [29] of logical qubits. Although our protocol is based on the pair matching of errors as the quantum ECs in toric code models [30,31], we solely focus on removing the errors from measurement data and identifying correlations between the parity flips. A comparison with previous quantum error-correction protocols is provided in Appendix C 6. Last but not least, our EC protocol is versatile enough to apply to other lattice geometry beyond the square lattice like Lieb and triangular lattices (Appendix E and Fig. 17).

IV. MEASUREMENT OF BRANE CORRELATORS

We turn our attention to the main result of this work, where we implement the EC to the experimental data and compute the brane parity correlator $\langle O_D\rangle$ across the MI-SF phase transition (Fig. 2). Upon applying the EC, we observe a dramatic increase of the $\langle\mathcal{O}_\mathcal{D}\rangle$ in the MI phase, and the parity correlator can well distinguish two phases even for the $L = 12$. The experimental results also show excellent agreement with QMC results after the error corrections. Compared to $\langle\mathcal{O}_\mathcal{D}\rangle$ before EC, the error-corrected values of the brane parity correlator are also much closer to that of the correlator at the zero temperature (obtained from QMC simulations) as expected. The free holes from thermal fluctuations are part of the errors in simulating the ground state of MI, which our EC method targets to correct. Thus, our EC effectively lowers the temperature of the snapshots. If the EC were perfect and could have removed all the uncorrelated errors, then the resulting brane parity correlator after the EC should agree with the zero-temperature values of the system with $\eta = 0$. However, in Fig. 2, we observe a small but noticeable gap between the error-corrected value (blue straight line) and the zero-temperature value (dark blue dotted line). The difference between the two is the result of the rare failure of correcting uncorrelated errors in close proximity to other parity flips (see Appendix D 1). The uncorrelated errors,

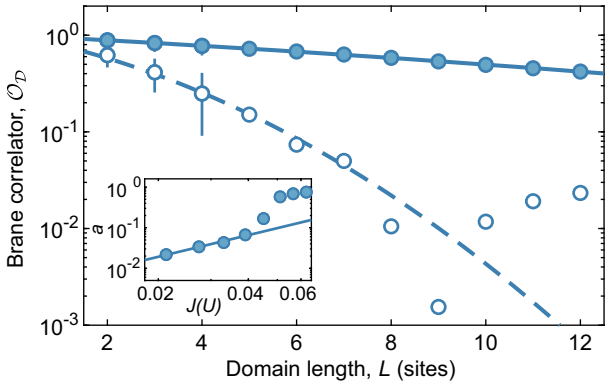

FIG. 3. Scaling of the brane parity correlator. Log plot of the brane parity correlator with domain length L at MI phase with $J/U = 0.0391$. Without the EC method (open symbol), the brane parity correlator drops quadratically with increasing domain length. On the other hand, the brane correlator with the EC method drops nearly linearly with the domain length. Inset: the exponential decay parameter a as a function of J/U. Solid line is a power-law fit curve with $a \propto (J/U)^{1.8}$, at an interval, $0.02 \leq J/U \leq 0.04$. The data are obtained over 40 independent experimental runs, and the error bar denotes one standard error.

which survived the EC, led to the underestimate of $\langle \mathcal{O}_D \rangle$. Nonetheless, we observe that the EC significantly enhances the signals of $\langle \mathcal{O}_D \rangle$, which consistently follows the trend of the zero-temperature values.

The effect of EC is also reflected in the scaling behaviors of $\langle \mathcal{O}_\mathcal{D} \rangle$ with respect to the domain length L. Consider the case without the EC. In this case, $\langle \mathcal{O}_\mathcal{D} \rangle$ is expected to scale as follows:

$$\log(\langle \mathcal{O}_\mathcal{D} \rangle) \sim -aL - bL^2,$$

in which the first term $\propto L$ is the expected perimeter law for $\langle \mathcal{O}_\mathcal{D} \rangle$ in MI [32]. Whenever the domain boundary intersects the short-ranged particle-hole pairs, the brane operator returns a value of $\mathcal{O}_\mathcal{D} = -1$ that exponentially suppress its expectation value with the perimeter length. The second term $\propto L^2$ is due to the uncorrelated holes. Such holes are uncorrelated and randomly occur in each site, and hence its overall effect on the $\langle \mathcal{O}_\mathcal{D} \rangle$ is proportional to the area of the domain $\mathcal{D}$. Indeed, our experimental data (Fig. 3) are well fitted with $a \approx 0.21(5)$ and $b \approx 0.034(9)$. Note that the fitted value b is not negligible compared to a. This explains why the bare measurement of $\langle \mathcal{O}_\mathcal{D} \rangle$ (Fig. 2) does not show any signals regardless of the underlying many-body states. On the other hand, when EC is implemented, we immediately find that the expected perimeter law is extremely well followed (Fig. 3). Here, the EC-assisted data are fitted with $a \approx 0.058(1) \gg b \approx 0.0012(1)$. We also observe that the decay coefficient a scales with tunneling energy $a \propto (J/U)^2$. This observation indicates the correlated particle-hole pairs in the MI phase from the quantum fluctuations, which is also represented in the parity correlation function $C(i,j) = \langle P(i)P(j) \rangle - \langle P(i) \rangle \langle P(j) \rangle$ (Appendix A).

Although the scaling behaviors of $\langle \mathcal{O}_\mathcal{D} \rangle$ can distinguish both MI and SF phases in a finite system size, the value of $\langle \mathcal{O}_\mathcal{D} \rangle$ itself cannot be used as an order parameter in the thermodynamic limit because of the perimeter law. Recently the generalized brane correlator has been proposed [14,15] to resolve this problem by considering the fractional version of the brane parity correlator,

$$\mathcal{O}^\theta_\mathcal{D}(r,L) = \left[\prod_{1 \leq x \leq r} \prod_{1 \leq y \leq L} P_{(x,y)} \right]^\theta,$$

where the angle $\theta = \pi/L^{-\alpha}$ depends on the domain length with a power-law exponent $\alpha \in [0,1]$. When $\alpha \geq 0.5$, the generalized brane correlator can have a finite value for MI in the thermodynamic limit and become zero in SF, serving as an order parameter for the MI [15].

The fractional parity correlator $\langle \mathcal{O}^\theta_\mathcal{D} \rangle$, however, cannot be evaluated from the standard parity-projected fluorescence imaging system since it requires the information of the number of occupations in each lattice site n_i. By using our EC method, we can evaluate the $\langle \mathcal{O}^\theta_\mathcal{D} \rangle$ even without additional experimental techniques to resolve the site occupation [33–36]. Since our error model can identify the correlated particle-hole pairs, we can statistically infer the site occupation n_i in the domain $\mathcal{D}$, and thus estimate the generalized brane correlator in the MI regime. It is based on the fact that the number fluctuations are small inside the MI, such that the n_i does not deviate much from its average $\bar{n} = 1$. To measure the generalized brane parameter, we first assign the correlated particle-hole pairs for a given parity snapshot with probability computed within our EC model Eq. (2). Then, to a given pair, the site occupation number is randomly specified by either a doubly occupied site $n_i = 2$ or an empty site $n_i = 0$ and evaluate the $\langle \mathcal{O}^\theta_\mathcal{D} \rangle$. Although the number fluctuations can become large in the SF phase, the generalized brane correlator is zero in the SF so that we can statistically measure the $\langle \mathcal{O}^\theta_\mathcal{D} \rangle$ across the SF-MI phase transition (Appendix F).

Figure 4 shows the EC-assisted measurements of generalized brane correlator. We observe that the error-corrected values fit well with the zero-temperature values inside deep Mott insulators [Fig. 4(a)], while the difference between the two becomes noticeable as the system approaches the SF. As in the case of brane parity correlators (Fig. 2), this is attributed to the rare failure of correcting uncorrelated errors in the EC, leading to the underestimation of the generalized brane correlator. Despite this, the fractional parity correlator with $\alpha = 0.5$, $\langle \mathcal{O}_\mathcal{D}{}^{\pi/\sqrt{L}} \rangle$, can well distinguish MI from SF and has a negligible dependence on the domain length in MI [Fig. 4(a)]. These results can be understood by noticing that the generalized brane correlator in the MI becomes $\langle \mathcal{O}^\theta_\mathcal{D} \rangle \simeq e^{-(\pi^2\theta^2/2)\langle \delta N^2 \rangle}$ within

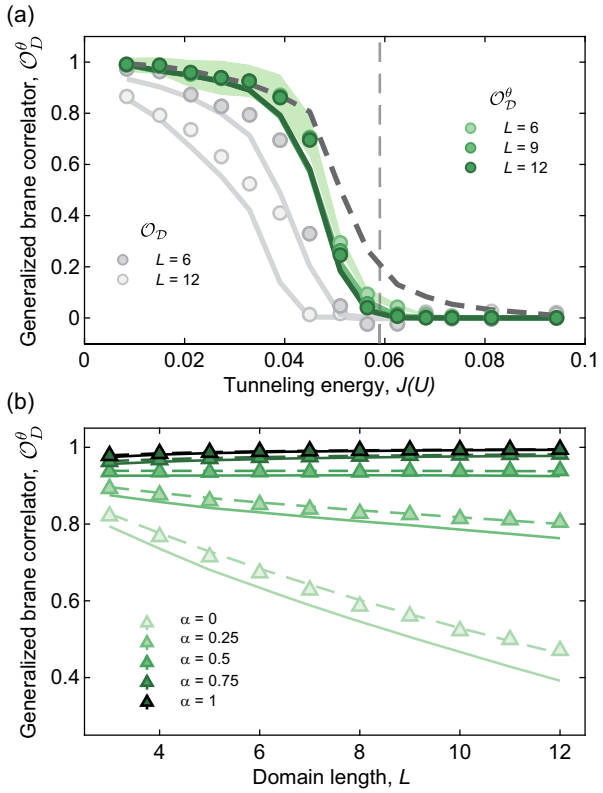

FIG. 4. Generalized brane correlator. (a) The generalized brane correlator with $\alpha = 0.5$ is drawn for different domain lengths $L = 6$–12. The generalized brane correlator for MI stays almost constant even at large system size $L = 12$. The solid lines represent the error-corrected values of the BH model with $\eta = 0.0277$ and $T = 0.083U$, and the dotted line represents the zero-temperature values of the system with $\eta = 0$. Both are obtained by QMC simulations (Appendix B). The gray dotted line represents the quantum critical point of the Bose-Hubbard model in 2D, $(J/U)_c = 0.059$ [25]. The data are averaged over 40 different experimental realizations, and the shaded area denotes the maximum standard error. (b) Domain length dependence of the generalized brane correlators at Mott insulating phase ($J/U = 0.027$) with different parameter $\alpha \in [0, 1]$. The integer parity correlator ($\alpha = 0$) decays with L, while the fractional parity correlators are domain size independent when $\alpha \geq 0.5$ for MI states.

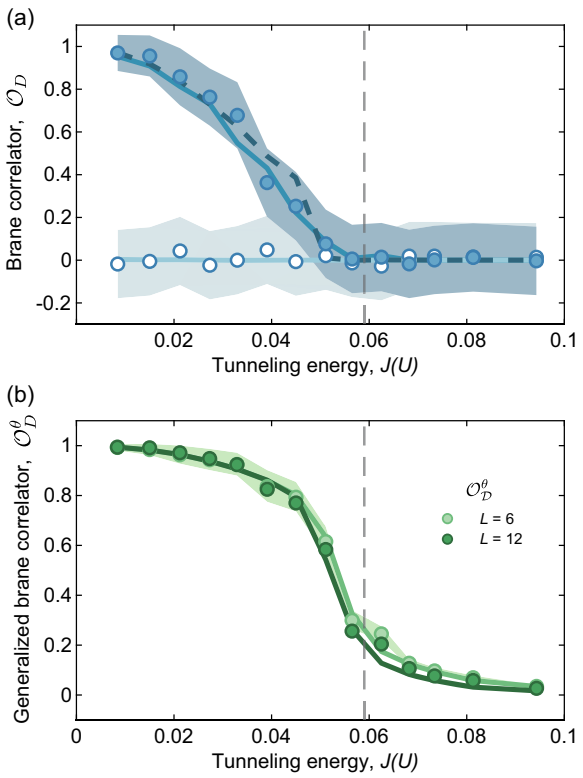

FIG. 5. Brane correlators with improved EC protocol. The improved EC protocol (Appendix D) is used to evaluate the brane parity correlator and generalized brane correlators. (a) Brane parity correlator with the domain size $\mathcal{D} = 12 \times 12$. The correlator of the experimental data before the EC (open circle). The error-corrected value of the experimental data (closed circle) well agrees with the error-corrected value (blue solid line) of the QMC simulation of the BH model at the experimental parameters $T = 0.083U$ and $\eta = 0.0277$. Notably, these error-corrected results show an excellent agreement with the zero-temperature QMC simulations of the BH model with $\eta = 0$ (dotted line). (b) The generalized brane correlators $\mathcal{O}_D^\theta$ with $\alpha = 0.5$ are drawn for different domain lengths $L = 6$ and $L = 12$ (green circles). Notably, the solid lines represent the zero-temperature extrapolations of the QMC simulations of $\mathcal{O}_D^\theta$ (Appendix B), which fit well with the error-corrected values of the experimental data. The shaded area represents the maximum standard error at $L = 6$.

a Gaussian approximation. Since the number fluctuations linearly increase with the domain length L in the MI (not shown), the angle $\theta = \pi/\sqrt{L}$ can normalize the brane correlator and remove the system size dependence. Indeed, varying the exponent α, we find that $\langle \mathcal{O}_\mathcal{D}^\theta \rangle$ show a negligible dependence on L for MI only for $\alpha \geq 0.5$ [Fig. 4(b)], which is consistent with the previous theory prediction [15]. While in the superfluid phase, the number fluctuations are much stronger, and the fractional parity correlator rapidly vanishes over the domain length. Consequently, the phase transition curve becomes sharper with increasing the domain length, and the quantum critical point can also be fairly well identified. The result confirms the recent prediction that $\langle \mathcal{O}_\mathcal{D}^\theta \rangle$ can be an order parameter of the MI phase in 2D [15].

Being extremely simple and computationally efficient, our EC protocol significantly enhances the signals of the brane parity correlators (Fig. 2) and the generalized brane correlators (Fig. 4), which are otherwise challenging to observe. On the other hand, we also noted that the error-corrected values of the brane correlators are generally smaller than the zero temperature values (Figs. 2 and 4) because the current protocol fails to detect rare errors lying close to other parity flips. This issue is actually easy to resolve. In our current protocol, to decide if a given parity flip is uncorrelated or not, we consider only a single possible pair of the parity flip with the largest correlation

Eq. (3). The better way to detect the error is to consider the multiple pairs of parity flips simultaneously in a single snapshot. This simple change, which is detailed in Appendix D, leads to further improvement of the brane correlators (Fig. 5), which now agree surprisingly well with the zero-temperature values. This signals that the improved EC protocol can detect the rare uncorrelated errors, which the original EC scheme could not detect. Of course, this improvement is not free and comes with more computational cost. Compared to the original EC scheme, the overall computational cost has a prefactor which is super-exponential in the number of pairs to be considered in each snapshot (but importantly not in the system size; see Appendix D 2 for details). Finally, we note that this improved protocol well exemplifies the flexibility of our EC protocol. The error detection (if we use the single pair or multiple pairing patterns) is only a single step in our full protocol. Depending on one's purpose and available computational resources, one can change and improve various specifics of our EC protocol to achieve the intended goals.

V. CONCLUSIONS AND OUTLOOKS

We present an error-correction method for a neutral atom quantum simulator using an optical lattice, which enables the measurement of nonlocal multipoint correlators in two dimensions. Our method is based on mapping the parity snapshot data of the Bose-Hubbard system to the spin configurations of a 2D Ising error model, whose properties can be calculated efficiently. The error model allows us to systematically compute the probability for the two holes to be paired, and thus to identify and remove uncorrelated holes from the experimental image. Using the error-corrected images, we can confirm that the brane parity correlator shows a clear perimeter scaling law to the relatively large scales. Moreover, we successfully measure the generalized brane correlators with negligible dependence on domain size L, which can serve as the order parameter for MI. Our work opens up a number of promising directions for further study. One possible extension is to explore the nonlocal order parameters of the topological phases, such as a Haldane insulator in an extended Hubbard model [10,37], gapped spin SU(N) chain [38], and Kitaev-Heisenberg ladder [39]. In particular, it will be interesting to generalize our EC method to the ultracold atom simulation of the Fermi-Hubbard model [12,36,40]. In these systems, the correlations in snapshot data between different spin species are essential in understanding the physics of many-body states. One may attempt to build an analogous $\mathbb{Z}_2 \times \mathbb{Z}_2$ error model to capture the correlated virtual excitations and uncorrelated errors of the Fermi-Hubbard model. Another immediate extension of our work is to apply our EC model to enhance the visibility of Wilson loop operators in quantum simulations of toric codes [4,16,41] as in Refs. [42,43]. In the toric code, the Wilson loop operators are nonlocal operators that can detect and diagnose the topological order [4]. Given the duality between the $\mathbb{Z}_2$ gauge theory and the Ising model [44], it seems natural to use our approach to improve the diagnosis of topological orders [16,41].

Note added. Recently, we became aware of an experiment that measures brane parity correlator in 2D MI phase [45].

ACKNOWLEDGMENTS

We acknowledge discussions with Immanuel Bloch, Timon Hilker, Yoon-Ho Kim, Hyukjoon Kwon, and Johannes Zeiher, and thank Byungmin Kang for sharing his implementation on stochastic series expansion QMC. We are funded by the Samsung Science and Technology Foundation under Projects No. SSTF-BA1702-06 and No. SSTF-BA2002-05. We acknowledge funding by the National Research Foundation of Korea Grants No. 2019R1A6A1A10073887, No. 2019M3E4A1080401, No. RS-2023-00207974, No. RS-2023-00208291, No. 2023M3K5A1094810, No. 2023M3K5A1094812, and No. 2023M3K5A1094813. J. H. is supported by the KAIST up program. G. Y. C. acknowledges support from the Institute of Basic Science of Korea under Project Code IBS-R014-D1. W. L. acknowledges the support of the Soseon scholarship. W. L. and G. Y. C. are also supported by the Air Force Office of Scientific Research under Award No. FA2386-22-1-4061.

APPENDIX A: EXPERIMENTAL SYSTEMS

1. Experimental sequence

Our experiments begin with loading the cold ^{7}Li atoms into a single plane of a blue detuned vertical lattice with 2.2 μm spacing [23]. Radial confinement is provided by an optical dipole trap along a vertical axis. Then, the magnetic field is ramped to $B = 730$ G, tuning the scattering length of the atoms to have $a = 400a_B$ (a_B is the Bohr radius), and evaporative cooling is performed by lowering the radial trap depth. To study the two-dimensional Bose-Hubbard model, we increase the lattice potential in the horizontal plane, where we observe a large-sized Mott insulator with 1200(100) atoms at $30E_r$. The $E_r = h^2/2ma_{lat}^2$ is the recoil energy, where h is the Planck constant, m is the atomic mass, and $a_{lat} = 752$ nm is the lattice constant. Lattice modulation spectroscopy is employed to calibrate the Bose-Hubbard parameters. The interband transition (s-band to d-band) spectroscopy determines the hopping matrix element J, and the on-site interaction energy U is given by measuring the Mott gap energy [46]. The temperature T and the chemical potential μ are determined by the density profile in the deep Mott insulator phase [8], which gives $k_BT/U = 0.08(1)$ and $\mu/U = 0.75(5)$, respectively. The k_B is the Boltzmann constant and $U \approx h \times 10$ kHz.

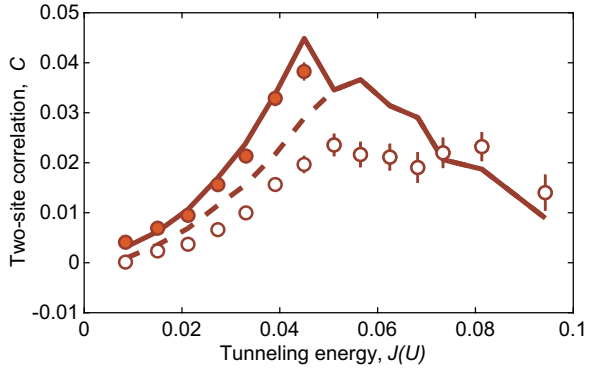

FIG. 6. Parity-projected density correlation. Experimental data are drawn with the error correction (closed symbol) and without the error correction (open symbol). The error bar represents the standard error of mean. The QMC simulation with random noise is drawn by using the error correction (solid line) and without the error correction (dotted line). The density correlation is maximum near the critical point.

2. Estimation of error rate η

To measure the loss during the imaging process, we took two consecutive images with 1 s exposure and 0.1 s interval. By comparing two images, we calculated the image fidelity by the Raman sideband imaging. The error during the imaging process mostly appears in the form of the loss with probability $\eta_{\mathrm{fid}} = 0.014(7)$. Another source for the uncorrelated error is the thermal excitation of the atoms. We measured the average filling of the Mott insulator to be $\bar{n} = 0.9713$. We compared it with the QMC simulation (see below) and computed that $\eta_{\mathrm{thermal}} = 0.008(3)$. The total uncorrelated error rate is $\eta = 0.028(4)$, consistent with $\eta_{\mathrm{thermal}} + \eta_{\mathrm{fid}}$ within the experimental uncertainties.

3. Input data of EC procedure

We use only the central region of the harmonic potential in the experiment, which can be regarded as the BH model with the mean filling $\bar{n} = 1$. For this, we first find the center of mass of each parity snapshot. We set the mass of each even or odd configuration by 1 or 0, respectively, in computing the center of mass. We then take a central region of each snapshot.

The size of the central region that we use varies depending on purposes. When we compute the brane correlators, we first take the central 20×20 size region out of the full system snapshots. Within this region, to compute the brane correlators of the size $L \times L$, we resample all possible $L \times L$ subpatches inside the 20×20 size snapshots. We then compute the expectation values of the brane correlators using these resampled subpatches. When we perform the EC on the snapshots, we instead take the center 23×23 snapshots to reduce the effect of the boundary. We then correct errors in the central 20×20 region of each 23×23 snapshot. All the data and plots in the main text are obtained by using ~40 independent snapshots in total.

We note that the statistical errors in the estimated brane correlators should not be given by the standard error, the standard deviation divided by the square root of the number of samples. This is because each brane correlator $O_{\mathcal{D}}$ is estimated by the mean value of the brane correlators of subpatches $\{\mathcal{D}_i\}$; i.e., $O_{\mathcal{D}} = (1/K)\sum_i^K O_{\mathcal{D}_i}$ with the number of the subpatches K. We note that $\{O_{\mathcal{D}_i}\}$ are mutually correlated due to their overlapping subpatches. In this case, the error of $O_{\mathcal{D}}$ exceeds the standard error. Importantly, the error of $O_{\mathcal{D}}$ is bounded by the maximum of the standard errors of $\{O_{\mathcal{D}_i}\}$. Thus, we use the maximum value as our estimation of the measurement error of $O_{\mathcal{D}}$ in the main text.

4. Two-site parity correlator

We measure the two-site correlator and the density fluctuations with different values of J/U and demonstrate the presence of particle-hole pairs in the Mott insulator. The two-site correlation is maximized near the critical point at $J/U = 0.059$ (Fig. 6). The experimental result is well matched with the numerical simulation result considering the harmonic curvature. Using the error-correction method, the two-site parity correlator is increased in the Mott insulator phase where the error correction is successfully done. In the SF phase, the error-correction method cannot distinguish the uncorrelated holes from the correlated holes, and the parity correlator remains the same.

APPENDIX B: QUANTUM MONTE CARLO SIMULATION

1. Finite-temperature QMC simulation

We use the directed loop QMC simulation proposed in Refs. [28,47]. The system size is set to be 50×50. The maximum boson occupation is set to be $n_{\max} = 3$. The harmonic curvature is set to be $\omega = 3.156 \times 10^{-2} U$ with the potential $V = \frac{1}{2}\omega r^2$. For each J/U, we calibrate the chemical potential so that the mean total boson number in QMC simulation matches that of the experiment. The total particle number is ~1220. The temperature is calibrated to $T = 1/12U$ so that we have $\eta_{\mathrm{thermal}} \approx 0.018$. We sample 3×10^4 snapshots to compute the expectation values of brane correlators.

2. Zero-temperature limit QMC simulation

By calculating the zero-temperature values of the brane parity correlator within the QMC simulation, we can test the performance of the error-correction scheme. These values are obtained by extrapolating the finite-temperature values to the zero temperatures. In Fig. 7(a), we plot the temperature dependence of the brane parity correlator for the 12×12 square domain. Here, we evaluate the brane

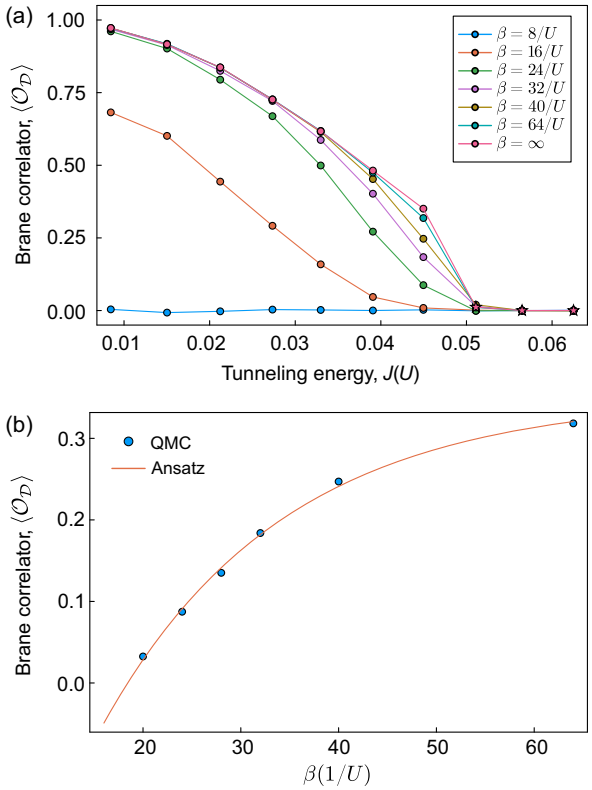

FIG. 7. Zero-temperature values of the brane parity correlators. (a) QMC simulation of brane parity correlators $\langle O \rangle$ with the domain size of 12×12 for various temperatures. (b) Extrapolation of brane correlators with $J/U = 0.045$ via the least square fit of the ansatz function $f(\beta) = ae^{-b\beta} + c$. In (a), data points marked by stars ($J/U = 0.0511$, 0.0565, 0.0625) are the cases where the brane correlators are too small to perform a systematic extrapolation. For those cases, we adopt $\langle O \rangle$ at $\beta = 96/U$.

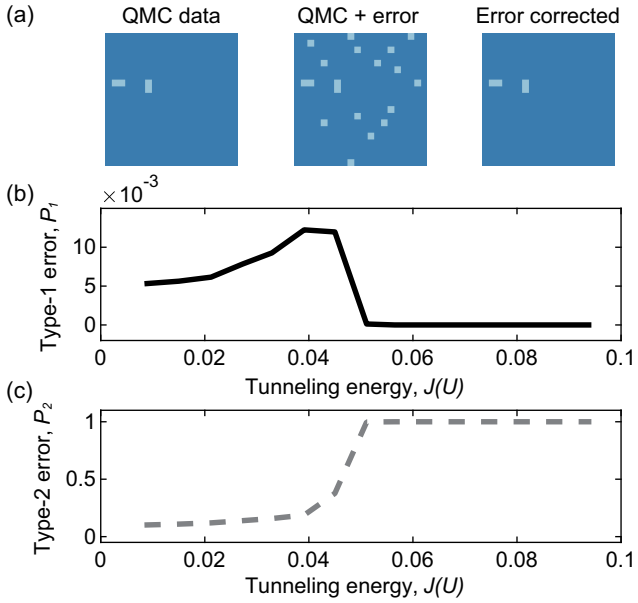

FIG. 8. (a) Error-correction estimation using the QMC data. Uncorrelated holes can be successfully removed using the EC method. From the QMC simulation, we estimate the incorrect decision of the error-correction scheme. (b) Type-1 error of the error-correction scheme. The type-1 error is the probability that we correct the wrong hole that does not come from the incoherent error source. We found that this probability is at most 1.2%, less than the experimental error rate of $\eta \approx 0.03$ from the thermal excitation and the imaging loss. It implies that the measured brane correlator in the MI is not from the overcorrection of the holes from the incorrect error-correction method. (c) Type-2 error of the error-correction scheme. The type-2 error represents the failure to correct the uncorrelated errors, and its rate is presented. The type-2 error in MI is much larger than the type-1 error. The error-correction method prefers not to correct the incoherent error when it is not certain. In the SF regime, the type-2 error is larger than 0.1 in the whole J/U values and it becomes 1.

parity correlator at a sequence of the temperatures up to $\beta = 1/T = 64/U$ and extrapolate its values to the zero temperature. The extrapolation to the zero temperature is carried out with the least square error optimization for the ansatz function $f(\beta) = ae^{-b\beta} + c$. We found that this ansatz agrees well for $J/U < 0.05$ as shown in Fig. 7(b). When J/U approaches the transition toward the superfluid or inside the superfluid, the values of the brane parity correlators are too small to perform a systematic extrapolation. For such cases, the brane parity correlators coalesce to zero within the statistical errors for the low temperatures. For those cases, we instead adopt the values at extremely low temperatures $\beta = 96/U$.

3. Error investigation with QMC data

We investigated the type-1 and type-2 errors of the error-correction method by correcting the added uncorrelated errors with the QMC simulation in Fig. 8. The probability of type-1 error is at most 1.2%, less than the experimental error rate of $\eta \approx 0.03$ from the thermal excitation and the imaging loss. It implies that the measured brane correlator in the MI is not from the overcorrection of the holes from the incorrect error-correction method. Contrarily, the type-2 error in MI is much larger than the type-1 error. The error-correction method prefers not to correct the incoherent error when it is not certain.

APPENDIX C: DETAILS OF ERROR CORRECTION

This appendix contains details of our EC methods, which were schematically discussed in the main text. Let us start with a brief note. If one wishes to develop a new EC method, there are a few (natural) requirements. First, the new EC scheme should be designed to reconstruct correlations appropriately between holes in each parity snapshot. In addition, it should be more efficient than the full simulation of the BH model. In this appendix, we will see that our error-correction scheme satisfies the two requirements nicely.

The rest of this appendix is organized as follows. First, we define the correlation between holes in a snapshot in Appendix C 1, which will be related to the spin-spin correlation function of the transverse field Ising model (TFIM) in Appendix C 3. We then show in Appendix C 2 that the correlation of TFIM can be classically and efficiently estimated. We next present our detailed arguments as to why the correlation of the BH model between two holes can be approximated by that of TFIM in Appendix C 3. To approximate the correlations of the BH model as that of the TFIM, a single parameter of TFIM, which is the "temperature" β of TFIM, should be calibrated. The calibration is done by matching the expectation values of the brane parity correlators of the BH model and TFIM, which is discussed in Appendix C 5. In Appendix C 4, we introduce how to efficiently compute the expectation values of the brane correlators in TFIM. In Appendix C 5, we finally discuss how to fix the parameter β of TFIM and complete our EC protocol. As a remark, we also comment on the relation of our EC method to the previous work in Appendix C 6

1. Correlation between holes

Here, we define what the correlation between holes in a snapshot means. Let us assume that we have a parity snapshot σ of a wave function $|\psi\rangle$. σ is a vector of 0 and 1 whose elements represent the parity of each site, i.e., $P_i = (-1)^{\sigma_i}$ (0 and 1 represent odd and even parities of the site occupation of the BH model, respectively). On top of this parity snapshot pattern σ, we want to introduce two parity flips (two holes) at i and j with $\sigma_i = \sigma_j = 1$. See Fig. 9. We will write the relation between σ and σ' as $\sigma' = \sigma \oplus 1_i \oplus 1_j$. Here, $\oplus$ is the modulo two summation, and 1_i is the unit vector having the unit ith element. Figure 9 illustrates the definition of $\sigma \oplus 1_i \oplus 1_j$.

The two parity flips $1_i \oplus 1_j$ in σ' can be introduced either from a paired virtual excitation of $|\psi\rangle$ or uncorrelated errors, e.g., free holes. The two holes are correlated if and only if they are introduced by a paired virtual excitation. The likelihoods of the two cases are given by

$$\mathcal{L}_{\text{corr}}(i,j|\sigma) = p(\sigma'), \qquad \mathcal{L}_{\text{err}}(i,j|\sigma) = p(\sigma)\eta^2, \quad \text{(C1)}$$

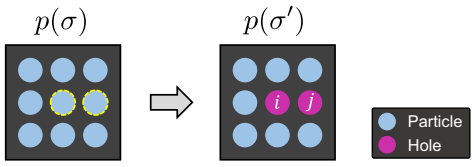

FIG. 9. Definition of $\sigma' = \sigma \oplus 1_i \oplus 1_j$. We introduce spin flips at the sites i and j.

with the probability $p(\sigma) = |\langle\sigma|\psi\rangle|^2$, the parity flipped snapshot $\sigma' = \sigma \oplus 1_i \oplus 1_j$, and the error rate η.

For a given parity configuration σ', we now ask the origin of the two parity flip. We may answer this question by comparing the two likelihoods. More precisely, we may conduct the maximum likelihood test: the two holes originate from uncorrelated errors if and only if $\mathcal{L}_{\text{corr}} < \mathcal{L}_{\text{err}}$. Equivalently, we may compare $\sqrt{p(\sigma')/p(\sigma)}$ with η. To simplify the notation, we will define $f(i,j|\sigma) \equiv \sqrt{p(\sigma')/p(\sigma)}$. We interpret that $f(i,j|\sigma)$ measures how easy it is to introduce a parity flip 1_i or 1_j on σ via a virtual particle-hole pair excitation, which will be compared to the uncorrelated errors.

In general, a snapshot σ has more than two holes, so each hole can pair with one of the other holes or can be left uncorrelated. In this case as well, we will conduct the maximum likelihood test per each parity flip. More precisely, for a given hole of σ at the site i, we first compute $f(i,j|\sigma \oplus 1_i \oplus 1_j)$ for all the other holes at the site j. We then compare its maximum value with the error probability η. The hole at the site i is uncorrelated if and only if

$$\max_j f(i,j|\sigma \oplus 1_i \oplus 1_j) < \eta. \quad \text{(C2)}$$

Note that since the number of holes in a snapshot is $\sim O(L_x L_y)$, the number of computations of $f(i,j|\sigma)$ for each snapshot scales $O(L_x^2 L_y^2)$. Thus, if $f(i,j|\sigma)$ is hard to compute, then we may not be able to conduct the maximum likelihood test. In fact, the computation of $f(i,j|\sigma)$ requires the ratio between $p(\sigma)$ and $p(\sigma \oplus 1_i \oplus 1_j)$, which is almost equivalent to the full computation of the ground state wave function. Thus, the direct computation of $f(i,j|\sigma)$ for the error correction is not meaningful because it is already as expansive as the full simulation of the BH model. Hence, we instead approximate $f(i,j|\sigma)$ by its average:

$$f(i,j|\sigma) \approx \frac{1}{2}\mathbb{E}[f(i,j|\sigma)] = \frac{1}{2}\sum_\sigma p(\sigma) f(i,j|\sigma). \quad \text{(C3)}$$

Before explaining the factor $1/2$ in the above, we note that the above quantity measures how easy, on average, it is to introduce a parity flip at 0_i or 0_j on a typical snapshot of $|\psi\rangle$ via a virtual particle-hole pair excitation. This can be compared to the uncorrelated error rate η to perform the maximum likelihood test. We will also regard this quantity as the square root of the likelihood $p(i \leftrightarrow j)$ of the pair of the parity flips at the two sites i and j being correlated. In the next section, we will see that $\mathbb{E}[f(i,j|\sigma)]$ of the TFIM is equivalent to the spin-spin correlator, which can be easily computed. Hence, the maximum likelihood test can be done classically efficiently.

The factor of $1/2$ in Eq. (C3) comes from the fact that we always choose a pair of parity flips in a snapshot σ' and try to reconstruct σ via undoing the virtual particle-hole excitation between the two sites. This introduces an ordering between snapshots, and the ordering can be approximately encoded by the condition $p(\sigma) > p(\sigma')$. This condition comes from the fact that the introduction of a virtual particle-hole excitation in MI requires finite energy cost, so the probability assigned on σ' is typically smaller than that on σ. Then, the average of $f(i,j|\sigma)$ over configurations satisfying $p(\sigma) > p(\sigma')$ is given by

$$\begin{aligned}&\sum_{p(\sigma)>p(\sigma')} p(\sigma) f(i,j|\sigma)\\ &= \sum_{p(\sigma)>p(\sigma')} \sqrt{p(\sigma)}\,\sqrt{p(\sigma')}\\ &= \frac{1}{2}\sum_{\sigma} \sqrt{p(\sigma)}\,\sqrt{p(\sigma')} = \frac{1}{2}\mathbb{E}[f(i,j|\sigma)]. \end{aligned} \tag{C4}$$

Here, the sum over σ satisfying $p(\sigma) > p(\sigma')$ is equivalent to the sum over all possible σ with $1/2$ factor.

The validity of our approximation above can be confirmed explicitly in the perturbative regime. Let us assume that we have a snapshot σ' of a MI state having a single pair of particle-hole excitations in a local region (see Fig. 10). Then, the probability of getting σ' is much smaller than that of the configuration σ. In addition, the probability of getting the snapshot σ from the ground state is almost equal to one. Also probabilities for getting other configurations are negligibly smaller than $p(\sigma)$ in the same reasoning. Thus,

$$\sum_{p(\tilde{\sigma})>p(\tilde{\sigma}')} \sqrt{p(\tilde{\sigma})}\,\sqrt{p(\tilde{\sigma}')} \approx \sqrt{p(\sigma')} \approx f(i,j|\sigma). \tag{C5}$$

In other words, we have $f(i,j|\sigma) \approx \frac{1}{2}\mathbb{E}[f(i,j|\sigma)]$.

2. Efficient calculation of correlation via TFIM

Here, we show how the correlation between the two parity flips can be calculated efficiently via mapping to transverse field Ising model. The ground state of TFIM that we will consider is given by the following imaginary-time evolved wave function:

$$|\psi\rangle = \frac{1}{\sqrt{\mathcal{Z}}} e^{\beta \sum_{\langle i,j\rangle} X_i X_j}|0\rangle, \quad \text{with} \quad \mathcal{Z} = \langle 0| e^{2\beta \sum_{\langle i,j\rangle} X_i X_j}|0\rangle. \tag{C6}$$

Note that there is only one single free parameter β. The free parameter will be tuned to match the statistical nature of the parity snapshots of the BH model. Its parent Hamiltonian is given as [26]

$$H = \sum_i Q_i, \quad \text{with} \quad Q_i = -Z_i + e^{-2\beta \sum_{i\in l} X_{l_1} X_{l_2}}. \tag{C7}$$

For small β, it becomes the conventional TFIM. This model also has the paramagnetic and ferromagnetic phases at roughly $2\beta_c = 0.441$, which is the critical temperature of the classical 2D Ising model.

One particularly important property of $|\psi\rangle$ is that it is a "classical" wave function; i.e., all the coefficients of $|\psi\rangle$ can be set to be positive and are given by the square root of the probability. Even more, a straightforward calculation shows that $\mathbb{E}[f(i,j|\sigma)]$ becomes the two-point $\langle X_i X_j\rangle$ correlator:

$$\mathbb{E}[f(i,j|\sigma)] = \sum_{\sigma} \sqrt{p(\sigma)}\,\sqrt{p(\sigma \oplus 1_i \oplus 1_j)} = \langle X_i X_j\rangle. \tag{C8}$$

Here, $\sqrt{p(\sigma)}\sqrt{p(\sigma')}$ with $\sigma' = \sigma \oplus 1_i \oplus 1_j$ is the product of the coefficients of $|\sigma\rangle$ and $|\sigma'\rangle$, and σ' is a configuration that can be obtained by applying spin flips on ith and jth sites. Thus, the sum of $\sqrt{p(\sigma)}\sqrt{p(\sigma')}$ over all configuration σ is equivalent to $\frac{1}{2}\langle X_i X_j\rangle$.

Next we show that $\langle X_i X_j\rangle$ is given by the two-point correlator $x_i x_j$ of the classical 2D Ising model, which can be efficiently computed from a single Monte Carlo simulation [48]:

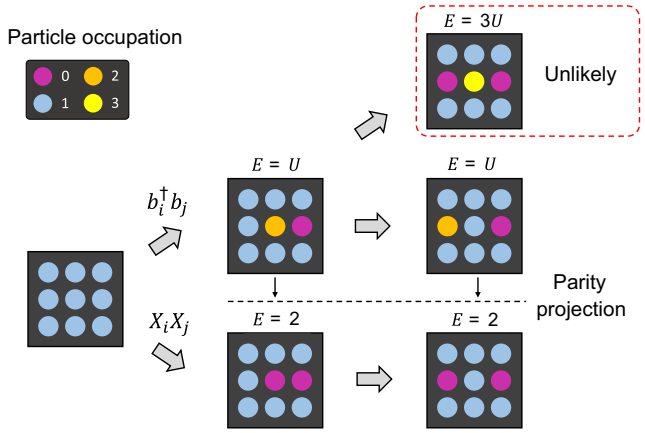

FIG. 10. Illustration on the perturbative analysis. In the case of BH model, when the two particle-hole pairs overlap, many of them overlap in a way that does not excite multiple particles due to the large energy penalty. Each parity snapshot of those low-energy configurations can be obtained by applying spin-flip $\sim XX$ terms at the same locations.

TABLE I. Mappings between BH model and TFIM. The mapping is exact deep inside the MI phase.

	BH (with the mean filling of $\bar{n}=1$)	TFIM
Creation of virtual excitations	Hopping term $b_i^\dagger b_j$	Ising term X_iX_j
Energy of excitations in deep MI	Interaction $n_i(n_i-1)$	Paramagnet term Z_i
Snapshot variable	On-site parity P_i	Spin-z Z_i
Nonlocal order parameter	Brane correlator $\prod_{i\in\mathcal{D}} P_i$	Domain wall operator $\prod_{i\in\mathcal{D}} Z_i$

$$\begin{aligned}\langle X_iX_j\rangle &= \frac{\langle 0|e^{\beta\sum_{\langle l,m\rangle}X_lX_m}X_iX_je^{\beta\sum_{\langle n,p\rangle}X_nX_p}|0\rangle}{\mathcal{Z}}\\ &= \frac{\prod_k(\frac{\langle+|_k+\langle-|_k}{\sqrt{2}})e^{\beta\sum_{\langle l,m\rangle}X_lX_m}X_iX_je^{\beta\sum_{\langle n,p\rangle}X_nX_p}\prod_q(\frac{|+\rangle_q+|-\rangle_q}{\sqrt{2}})}{\langle 0|e^{2\beta\sum_{\langle i,j\rangle}X_iX_j}|0\rangle}\\ &= \frac{\sum_x x_ix_je^{2\beta\sum_{\langle i,j\rangle}x_ix_j}}{\sum_x e^{2\beta\sum_{\langle i,j\rangle}x_ix_j}} = \langle x_ix_j\rangle_{\mathrm{Ising},2\beta}.\end{aligned}$$

3. Reasoning behind approximation by TFIM

Here, we provide intuition of why dynamics of virtual particles of the BH model can be well mimicked by that of TFIM. We summarize our mapping between the two models in Table I. To support the mapping, we will first show that the probability distribution of parity configurations of BH model (with the mean filling of $\bar{n}=1$) and TFIM can be matched within the perturbative regions (away from the deep MI). This implies that $\mathbb{E}[f(i,j|\sigma)]$ can also be matched for the two models. In addition, we will also argue that the dynamics of virtual particles of BH model and TFIM are qualitatively similar. Finally, we show that expectation values of diagonal observables of the both models, i.e., observables in Z or parity basis, can be matched simultaneously by properly tuning β.

First, we note that the wave functions of both models at the stable fixed points give the same probability distribution for the spin σ or number parity P at each site:

$$\begin{aligned}&\text{MI in the BH, or paramagnet in the TFIM:}\\ &\quad p(0)=0 \quad\text{and}\quad p(1)=1,\\ &\text{SF in the BH, or ferromagnet in the TFIM:}\\ &\quad p(0)=\frac{1}{2} \quad\text{and}\quad p(1)=\frac{1}{2}.\end{aligned} \tag{C9}$$

The spin and the number parity are related by $P=(-1)^{\sigma+1}$. Second, the energy cost of introducing a pair of two excitations X_iX_j or $b_i^\dagger b_j$ to the fixed-point configuration $\sigma=0$ or $P=1$ of MI is given by $\Delta E=2$ in TFIM or $\Delta E=U$ in BH, respectively. Note that each boson hopping operator has a direction, while each Ising operator has no direction. Thus, one may expect that some perturbative configurations made by boson hopping operators cannot be made by Ising operators. However, in the deep MI, the energy cost of making such a configuration is large. For example, $|030\rangle$ (written in the number basis) can be made by applying $b_2^\dagger b_1$ and $b_2^\dagger b_3$ operators on $|111\rangle$ (again written in the number basis). Obviously, the $|030\rangle$ state does not have the corresponding state in TFIM. However, its energy cost in the deep MI is $3U$, so it is unlikely to occur for large U. It means that their parity distribution in deep MI can be matched with the spin configurations in TFIM. Figure 10 illustrates this.

In addition, the two-point correlators $\langle b_i^\dagger b_j\rangle$ (in BH model) and $\langle X_iX_j\rangle$ (in TFIM), which measure how easy it is to introduce a pair of virtual particle-hole pairs, behave similarly. First, they both exponentially decay in the MI and paramagnetic phases; i.e., $\langle b_i^\dagger b_j\rangle$ and $\langle X_iX_j\rangle$ follow $\sim e^{-|i-j|/\xi}$ with the correlation length ξ. Second, they both converge to finite numbers in the SF and ferromagnetic phases.

Based on these facts, we expect that the values of the observables of both the models, which are diagonal in the parity basis or spin-Z basis, can be well matched. A particularly interesting observable in both sides is the brane parity correlator $\prod_{i\in\mathcal{D}} P_i$ in BH model, which is equivalent to the domain wall operator $\prod_{i\in\mathcal{D}} Z_i$ in TFIM. The brane parity correlator decays exponentially in $|\partial\mathcal{D}|$ in MI (which corresponds to the paramagnetic phase in TFIM) and superexponentially in $|\partial\mathcal{D}|$ in SF (which corresponds to the ferromagnetic phase in TFIM). As the diagonal observables can be well matched in both sides, we may calibrate

the parameter β of TFIM by matching the expectation value of the brane parity correlator in both sides. In the next section, we will discuss how to efficiently compute the expectation values of the domain wall operators of TFIM in more detail. This will be used to calibrate β. Note that in principle we can match expectation values of a set of brane parity correlators with multiple domain sizes. By doing so, we can expect to better match the scaling behaviors of the brane parity correlators on both sides, which will eventually lead to the better EC performance. However, we will use only a single domain size of $|\mathcal{D}| = 3 \times 3$ to calibrate for simplicity.

4. Brane parity correlator of TFIM

Here, we discuss how to compute the brane parity correlators, or equivalently domain wall operator of TFIM. The brane parity correlator of the BH model is computed from the parity snapshots generated by our quantum simulator. The brane parity correlator of TFIM is computed from classically generated spin-z snapshots. Below, we discuss in more detail how to classically generate spin-z snapshots of TFIM.

First, let us consider the expansion of the wave function Eq. (C6):

$$|\psi\rangle = \sum_{n=0}^{\infty} \frac{\beta^n}{n!} \left(\sum_{\langle i,j \rangle} X_i X_j \right)^n |0\rangle = \prod_{\langle i,j \rangle} \sum_{n=0}^{\infty} \frac{\beta^n}{n!} (X_i X_j)^n |0\rangle. \tag{C10}$$

We note that spin configurations of $|\psi\rangle$ can also be described by link configurations:

$$|l\rangle_{\text{link}} = \prod_i \frac{\beta^{l_i}}{l_i!} (X_{l_{i_1}} X_{l_{i_2}})^{l_i} |0\rangle. \tag{C11}$$

Here, l_{i_1} and l_{i_2} are sites connected by the link l_i. Each spin σ_i at the ith site is given by the parity of the total number of links connected with the site, i.e., $\sigma_i = \sum_{l \in i} l_i \pmod 2$. These link configurations are redundant, and multiple link configurations can give a single spin configuration. We will refer to the set of all links that give rise to a spin configuration σ as link(σ). The probability for a configuration $|\sigma\rangle$ is then given by

$$p(\sigma) = \left(\sum_{l \in \text{link}(\sigma)} \prod_i \frac{\beta^{l_i}}{l_i!} \right)^2 = \sum_{l,s \in \text{link}(\sigma)} \prod_{i,j} \frac{\beta^{l_i}}{l_i!} \frac{\beta^{s_j}}{s_j!}. \tag{C12}$$

We can think of it as products of two classical systems with link variables l and s whose statistical weights are $\beta^n/n!$, where n is the degeneracy of each link. We note that since l and s give the same spin configuration σ, they should be related by a closed loop of links o, which does not change the spin configuration.

Our next step is to develop a classical Monte Carlo scheme simulating Eq. (C12). The classical MC protocol is composed of two updates: the parity update and the loop update. The parity update changes σ by adding or removing one link term from a link. The statistical weight associated with adding (removing) a link term to l_i and s_i is $\beta^2/(n_{l_i}+1)(n_{s_i}+1)$ $(n_{l_i} n_{s_i}/\beta^2)$. The loop update adds a closed loop of links on either l or s. To do so, we first choose arbitrary position and inject a worm which propagates along links. It adds (removes) a link term on each link based on the statistical weight $\beta/(n+1)$. The worm moves until its head and rear meet. We find that two update schemes are sufficient to simulate $p(\sigma)$ of $|\psi\rangle$.

5. Calibration of β

Here we elaborate on how to calibrate the parameter β of the Ising wave function $|\psi\rangle$. Overall, we calibrate β by matching the expectation value of the domain wall operator of $|\psi\rangle$ with the expectation value of the brane parity correlator computed from error-corrected parity snapshots. It consists of a few independent steps. First, for some window of β, we compute the domain wall operator of $|\psi\rangle$ at β. Second, for the same window of β, we perform the EC on the parity snapshots using the correlator $\langle X_i X_j \rangle$. Then, we choose the optimal β where the error-corrected brane parity correlator agrees with the value of the domain wall operators. The overall process of the calibration is illustrated in Fig. 11.

Step 1: Calculation of domain wall operator in TFIM. In the calibration process, we need to find β that matches the value of the brane parity correlator of BH model with the value of the domain wall operator of TFIM. To accurately determine the self-consistent β, it is crucial to explore β with small intervals, even within the SF phase. However,

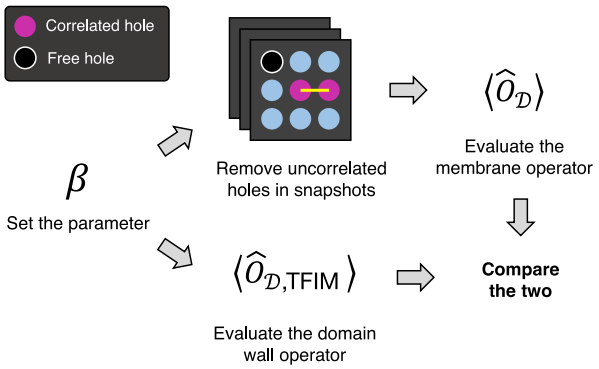

FIG. 11. Overall process of calibrating β. We attempt to find β that matches $\langle \hat{O}_{\mathcal{D}} \rangle$ and $\langle \hat{O}_{\mathcal{D},\text{TFIM}} \rangle$. For each β, we compute $\langle \hat{O}_{\mathcal{D}} \rangle$ from error-corrected parity snapshots of BH model and $\langle \hat{O}_{\mathcal{D},\text{TFIM}} \rangle$ from TFIM. We scan β and find the value that matches the two optimally.

this demands extensive Quantum Monte Carlo simulations for computing the domain wall operators. This makes the EC protocol less efficient. Thus, we perform a rough scan of β to compute the domain wall operators and then interpolate them using a (cubic) polynomial $f(\beta)$.

It is important to note that this approach inevitably introduces a cutoff on β, i.e., it cannot be greater than a certain value β_*, which is a zero of f. This is particularly important in SF phase due to the following reasons. First, let us assume that we do not introduce any cutoff and $\langle O_{\mathcal{D}}\rangle$ is small, i.e., SF states. Then, β becomes extremely sensitive to the exact numeric values of $\langle O_{\mathcal{D}}\rangle$. It means that if $\langle O_{\mathcal{D}}\rangle$ is not sufficiently accurate compared to the experimental error bars, then β cannot be determined. To fix β in this case, we introduce a cutoff on J/U and corresponding β. This make β not exceed the cutoff even when $\langle O_{\mathcal{D}}\rangle$ is uncertain. Second, since we compute the brane parity correlator to distinguish the two phases of BH model, practically we do not need to increase β above $\beta_c \approx 0.22$ if the brane parity correlator is already vanishing.

Step 2: Calculating $\langle X_i X_j\rangle$. We compute the two-point correlator $\langle X_i X_j\rangle$ using the classical Ising correlator $\langle x_i x_j\rangle_{\mathrm{Ising},2\beta}$ as discussed in Eq. (C9). To compute the Ising correlator, we perform the classical Monte Carlo simulation proposed in Ref. [48] on 64×64 square lattice, which is sufficiently larger than 20×20 experimental parity snapshots. We note that a single Monte Carlo simulation is sufficient to compute $\langle x_i x_j\rangle_{\mathrm{Ising},2\beta}$ for all i, j.

Step 3: Search for optimal β. We find the optimal β by comparing expectation values of the brane parity correlator in BH model and the domain wall operator in TFIM. For typical J/U, we can find a unique $\beta\neq 0$ that perfectly matches the two observables. In this case, we can unambiguously fix β and error correction is self-consistent. However, it is also possible that there are multiple self-consistent solutions $\beta\neq 0$ that perfectly match the observables in the two sides. In this case, we choose the minimum β, which maximally (but not entirely) removes holes in a self-consistent way. In addition, for small J/U, there could be no consistent solution except the trivial one with $\beta=0$, which eliminates all holes in snapshots. Although the trivial solution is also a self-consistent solution, it is physically a wrong choice since it removes all correlated holes. Thus, we do not set $\beta=0$. Instead, we choose the optimal β that do not remove all holes.

6. Relation with previous QEC methods

Here we present a brief comment on the relation of our EC method to the previous works. We will mainly compare our EC method to quantum EC protocols on the toric codes [29–31]. We first briefly review the quantum error-correction protocols in the toric code. We then compare them with our method. In the toric code, the errors always occur in pairs, and they may propagate far from each other. The QEC then attempts to pair these errors from the measurement data and remove them from the wave functions by performing proper quantum operations. In this process, it is important to define properly how the pair of errors are correlated. Dennis and Kitaev [29] assigned an error probability on each link of the toric code and mapped the QEC problem to the problem of finding the minimum energy configuration of the random bond Ising model. The (free) energy minimization problem is then mapped to other mathematical problems, such as the minimal weight perfect matching (MWPM) problem in graph theory, which can be efficiently solved [30,31]. Note that these methods can be used to detect correlated errors in our setup. One can also identify uncorrelated measurement errors by repeated measurements. In summary, QEC protocols target to identify and correct both the uncorrelated and correlated errors on quantum states. In this respect, one may find certain similarity between our EC method and the QEC protocols. However, there are several important differences.

First of all, we note that pairs of the parity flips in the parity snapshots of the MI are not errors that should be removed. Instead, we use this information to isolate and remove the uncorrelated holes, which will have no partner in the snapshot. The correlation between the parity flips also provides an estimate for the number fluctuations, from which we can evaluate the generalized brane correlators. In this regard, the goal of our method and that of the QEC protocols are different.

In addition, the QEC protocols for the toric code cannot perform the tasks that we need to do in our setup. To better appreciate this, we remind that the QEC protocols concern how to find the single most probable pairing pattern between the errors. This is legitimate for the QECs, which have to determine a pairing configuration and correct them. However, this does not take other probable patterns into account, which may appear in our problem. On the other hand, our EC method takes other probable patterns into account by finding and keeping the probability of each pair of holes in a parity snapshot to be correlated. By doing so, our method can pair long-ranged parity flips, which are hardly found by QEC protocols but relevant to our purpose. Holes in a parity snapshot could be correlated even when they are not nearby. In particular, such a long-ranged correlation gives a scaling of the brane correlator super-exponential in the perimeter of the membrane in the SF phase. This scaling would not be well captured by QEC protocols, for example, the MWPM, which pairs parity flips locally. On the other hand, our method can capture the scaling well as demonstrated in the main text.

7. Why does our EC protocol work?

The goal of the EC is to compute the "true values" of brane correlator within a bounded domain. Here, true values means the brane correlators of models without errors at the zero temperature. In Appendix F, we

argue that this is equivalent to computing the density of paired parity flips crossing the boundary of the domain without errors. We note that the paired parity flips can originate from quantum correlation or uncorrelated errors (when the EC wrongly assigns the pairing to the errors). Unfortunately, no matter how technically advanced an EC protocol can be, it is impossible to completely avoid true negatives, decisions that interpret an uncorrelated error as quantum correlation, and false positives, decisions that interpret quantum correlation as uncorrelated errors. This is because both uncorrelated error and quantum correlation can, in principle, give the same parity configuration.

Despite this, there are two possible resolutions to overcome this. First, one may design a proper strategy, i.e., a map from a snapshot with errors to an error-corrected snapshot, so that the frequencies of false-positive and true-negative occurrences coincide with each other. Second, instead of fixing the origin of each parity flip and performing removal of errors, it is also possible to give proper weight to each source, such as likelihood based on Bayesian analysis. In the main text, the former was chosen to evaluate the true values of the brand correlator. Below, we explain how the former method works.

To understand this, let us consider the simplest implementation: an error correction by introducing a cutoff length on each pair of parity flips. If the two parity flips are closer than the cutoff length l, then they are considered "correlated." Otherwise, they are "uncorrelated." We note that this method is simple in the sense that it examines only a single pair of parity flips at once. In this setup, an increment of the cutoff length l generally results in a decrement in the number of true-negative pairs. Conversely, considering parity flips caused by uncorrelated errors, we can also see that increasing the cutoff length leads to the increased number of false-positive pairs. Thus, there is a cutoff length that matches the occurrences of true negatives and false positives, Fig. 12, when η is small enough. Hence, the only task left for us to do is to find this appropriate cutoff l for the given experimental error rate and correlation length, from which we can evaluate the density of paired parity flips (crossing the boundary) and also the true values of the brane correlators. This is achieved by an appropriate error model, i.e., Ising model in our case, and the maximum likelihood test.

In deciding the appropriate cutoff length l, there are two important scales to consider: the error rate and the correlation length of the Bose-Hubbard model. The error rate is a value that can be estimated independently in the experiment. However, the direct measurement of the correlation length of the BH model is as difficult as estimating the true brane correlator. Therefore, to find the correlation length, we initially assume some suitable correlation length and then check whether the calculated pair density within the EC scheme is consistent with the assumed correlated length. To perform this test, we employ the Ising model as a proxy to find the cutoff length with which the pair density, equivalently the brane correlator, estimated within the EC method aligns with those of the Ising model.

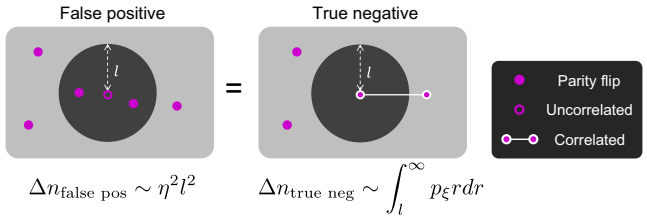

FIG. 12. Pictorial representation of false positives and true negatives in EC. Here, l is the cutoff length of the pair distance, which is roughly the order of the correlation length. Pairs having a length greater than l are regarded as uncorrelated. The empty circles are the uncorrelated errors, originating from various imperfections like thermal fluctuations or measurement errors. The circles linked by lines are parity flips generated by quantum fluctuations. The left-hand figure shows the false-positive decision where pairs generated by uncorrelated errors are judged to be correlated. Here, η is the uncorrelated error probability. The right-hand figure shows the true-negative decision where a pair generated by quantum correlation is judged to be uncorrelated. $p_\xi(r)$ is the probability of pairs with the length r generated by quantum fluctuations with the correlation length ξ. The error-correction method attempts to find the cutoff length l that balances the occurrences of false positives and true negatives.

APPENDIX D: IMPROVEMENT OF ERROR CORRECTION

Here, we discuss the limitations of the most straightforward implementation of the EC protocol and the ways to improve it. Specifically, we will present why the EC scheme underestimates the brane correlator in Mott insulators and the upper bound for the error-corrected values of the brane parity correlators. We then suggest their possible improvements.

In terms of notation, here is a small note. In this appendix, our original EC protocol (explained in the main text) will be called the "single-pair EC scheme" and the improved EC protocol (that we will introduce in this section) will be called the "multipair EC scheme" for obvious reasons, as will be seen soon. If not mentioned explicitly, the EC protocol always means the original scheme, namely the single-pair EC.

1. Limitation of original EC and upper bound of brane parity correlators

There are two main limitations in our original EC scheme. We will separately discuss them below.

a. Discreteness of lattice model

The first limitation arises from the discrete nature of our EC scheme. As discussed in Appendix C 7, the EC method

attempts to find the cutoff length that matches the number of true negatives and false positives. However, since we are considering a lattice model, the length of the pair should be discrete in unit cell size. For example, the nearest neighbors are spaced by 1, and the second nearest neighbors are spaced by $\sqrt{2}$, etc. On the other hand, the tuning parameter β in our Ising error model is continuous, resulting in the optimal cutoff length also being continuous. Thus, balancing between these two tensions, instead of finding the optimal cutoff length (which may not be discrete), what we can do at best is to adopt the discrete cutoff length closest to the optimal one. There is another related, important point to this discreteness of the lattice model: the minimum allowable cutoff length, which is set to be unity. The rationale behind this is that if the cutoff length were allowed to be less than the unit lattice spacing, then the EC invariably removes all parity flips for whatever the ratio of the Hubbard parameter J/U and the error rate, which is undoubtedly wrong.

These together lead to a mismatch between the number of true negatives and false positives. Notably, in deep Mott insulators, the discrete nature of the cutoff length results in the overestimation of false-positive pairs. This is because of two reasons. First, the density of true-negative pairs is vanishingly small. The correlated pair excitations are typically closest (within several unit cell scale) to each other, and hence the event that the EC wrongly regards them to be uncorrelated is unlikely. Second, the density of false-positive pairs is, however, finite η^2 with the error rate η. This is because there can be very rare events, where the uncorrelated errors accidentally occur right next to each other. If such occurs, then our EC would regard them as correlated because they are within the cutoff length. One important consequence of this mismatch is the underestimation of the brane parity correlators, whose upper bound can be derived analytically. Let us comment on this first before we move to the second limitation of our EC protocol.

b. Upper bound for brane parity correlator

The mismatch leads to an underestimation of the brane correlator because the false-positive pairs crossing the boundary give parity fluctuations within the domain. The degree of the underestimation is determined by the occurrence $n_{\text{false pos},\partial\mathcal{D}}$ of such false-positive pairs $c\eta^2|\partial\mathcal{D}|$ with the length of the domain boundary $|\partial\mathcal{D}|$ and the link multiplicity constant c which depends on lattice geometry. For the square lattice, the multiplicity constant is given by one. More precisely, the value of the reconstructed brane correlator is upper bounded by w times the value of the true brane correlator, where w is given by

$$w = \mathbb{E}[(-1)^{n_{\text{false pos},\partial\mathcal{D}}}]. \tag{D1}$$

Notably, this upper bound is always satisfied and almost saturated deep inside the Mott insulator. See, for example, Figs. 13 and 17.

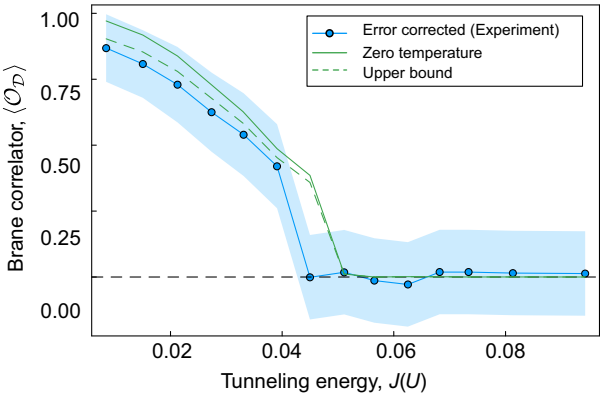

FIG. 13. The upper bound of error-corrected brane parity correlators with 12×12 domain recovered by the single-pair error-correction scheme. The blue circles represent error-corrected brane correlators estimated from experimentally measured parity snapshots. The green solid line represents the zero-temperature extrapolated brane correlator from QMC simulations (see Appendix B). The dashed line is an upper bound of error-corrected brane correlators, which are given by w times of the values of the zero-temperature brane correlators. Here, w is given by 0.93 for the square lattice with the uncorrelated error rate $\eta = 0.0277$.

c. Insufficient information of single-pair EC protocol

The second limitation of our EC is that it determines whether a pair is correlated or not by examining only a single pair of parity flips. It is easy to see that the original single-pair EC protocol used in the main text is valid when there is only one parity flip nearby, which can be potentially paired with. When there are more flips, one needs special care. In Fig. 14, there are three parity flips $\{0_a, 0_b, 0_c\}$. Here, we assume that 0_a and 0_b originate from the pair creation of particle and hole while 0_c originates from the measurement error. 0_a and 0_b form a true-negative pair that should be removed to correctly recover the density of the

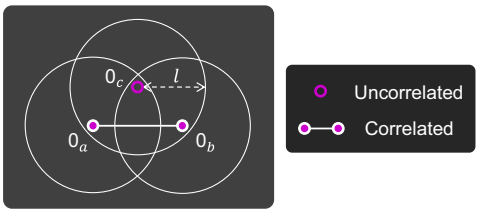

FIG. 14. A limitation of the original single-pair EC scheme. The figure illustrates a situation with three parity flips $\{0_a, 0_b, 0_c\}$. Among them, 0_a and 0_b are correlated, and 0_c is an uncorrelated error. The pair made by 0_a and 0_b is a true negative as its length is greater than l, the cutoff length. However, due to 0_c, both parity flips are judged as "correlated." In addition, 0_c is also judged as correlated even without nearby uncorrelated parity flips. These decrease the occurrence of true negatives and increase the occurrence of false positives compared to what the single-pair scheme expects, leading to a mismatch between them.

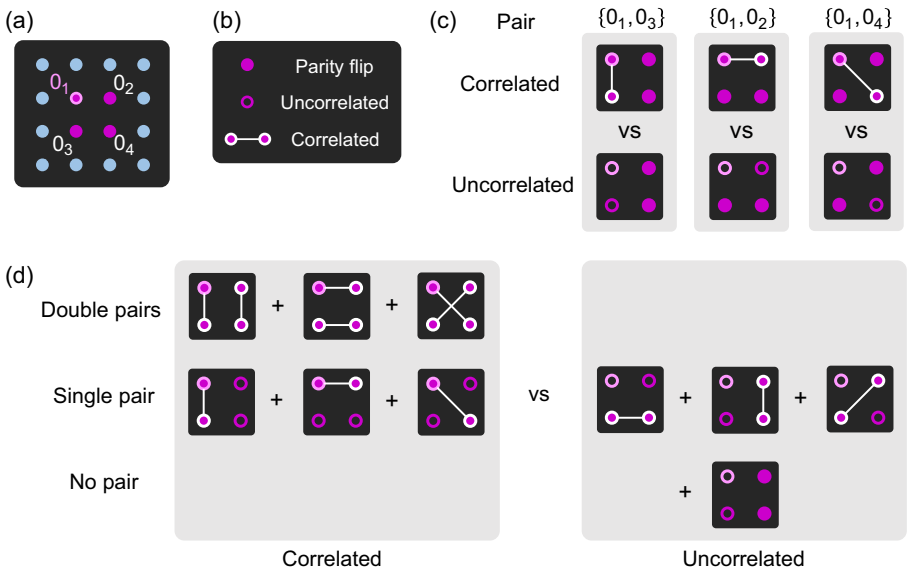

FIG. 15. Comparison of our original and improved EC protocols. (a) Input parity configuration for the EC protocols. Purple circles represent parity flips. There are four nearby parity flips $\{0_1, 0_2, 0_3, 0_4\}$. (b) Types of parity flips. Each parity flip is either correlated with another parity flip or uncorrelated. The first parity flip 0_1 is tested whether it is correlated or not by (c) the original protocol and (d) the improved protocol. (c) The original protocol examines the likelihoods of single pairs including 0_1 to estimate its correlation. (d) The improved protocol examines the likelihoods of all possible pairing patterns of the input parity flips to reconstruct the correlation of 0_1.

pair of parity flips. However, since each of all three can find at least another flip within the cutoff length, they will be regarded as correlated within our EC protocol. This prevents true-negative identifications of 0_a and 0_b, while it also leads to false-positive identification of 0_c. Eventually, this results in an imbalance between true negatives and false positives in our EC protocol. Consequently, the brane correlator is underestimated by this process. For small J/U and η, obviously this issue is not significant because each parity flip is rarely located nearby other parity flips. In this regime, the single-pair EC method recovers the true values of the brane correlator well. However, as J/U and η increase, a parity flip will more likely have several neighbor flips and could be correlated with more than one other parity flip. This increases the occurrence of false positives and decreases the occurrence of true negatives, which results in the underestimation of the brane correlator.

2. Improved protocol: Multipair EC scheme

We introduce a generalization of our original single-pair EC method, which greatly improves its performance. The original EC method, as explained in the main text and above, utilizes information about the correlation of a single pair. On the other hand, the multipair EC method generalizes it to consider all possible pairing and uncorrelated error configurations of locally clustered parity flips (see Fig. 15). We first present a basic picture of how this improved scheme works and then present the technical implementation.

a. Basic picture

Even though here we will develop a new EC protocol which takes multiple pairs of parity flips into account, the goal is the same as the original single-pair EC protocol: we want to identify whether a given parity flip is an uncorrelated error or not. If it is not an error, then we also need to determine with which parity flip it is correlated. Nonetheless, there is an important difference: In this improved EC scheme, we will also consider how the nearby flips are paired and take this into account when we assign the probability for a given parity flip to be correlated or not.

Let us illustrate how this improved EC works in an example parity snapshot Fig. 15(a), where four adjacent parity flips $\sigma = \{0_1, 0_2, 0_3, 0_4\}$ appear simultaneously. Imagine that we attempt to ask if 0_1 is an uncorrelated error or not. It is not difficult to see that, to determine this, we also need to estimate well if the other flips $\{0_2, 0_3, 0_4\}$ are paired or uncorrelated. For example, if $\{0_3, 0_4\}$ are paired and 0_2 is uncorrelated, then 0_1 is also uncorrelated. See the right-hand panel in Fig. 15(d) for this possibility. Hence, to decide if a parity flip 0_1 is correlated or not, we will need to know if the other nearby flips are correlated or not, and how they are paired if they are correlated. Notably, there are multiple possible scenarios [Fig. 15(d)] that can give the same final parity snapshot configuration. They have different probabilities to occur.

Now, we note the following: We can estimate the likelihood if the given parity flip is correlated or uncorrelated, if we can evaluate the probabilities for each of these

pairing configurations. For example, for the given parity flip 0_1 in Fig. 15, if the sum of the probabilities for configurations in the left-hand side of Fig. 15(d) is larger than the sum of the probabilities for configurations in the right-hand side of Fig. 15(d), then 0_1 is naturally regarded as correlated. Even more, from the same information, we can also infer the probabilities for the flip 0_1 to be correlated with other flips. Note that this is the same information as the number fluctuations as explained in the main text, and it is the necessary information for evaluating the brane parity correlators.

Thus, to perform the EC task, we only need to calculate the probabilities for the parity snapshot configurations for various possible pairings and uncorrelated errors. Note that this is readily done, because we already know from the single-pair EC protocol that the probability for each pairing between two parity flips is given by the Ising spin-spin correlator $\sim\langle X_i X_j\rangle^2/4$ and the probability for each uncorrelated error is η. All we need to do is to multiply these factors properly to correctly evaluate the probability for each configuration.

b. Relation with the original single-pair EC scheme

The above discussion makes it clear that the multipair EC scheme is just a generalization of the original single-pair EC scheme. The only difference between the two is the way to compute the probability of a given parity flip. In the single-pair EC scheme, we consider the probability of one pairing associated with the given parity flip. In the multipair EC scheme, we take the possible pairing configurations of other nearby flips into account, too. This is summarized in Fig. 15. Note that this is only a single step in EC and independent from other steps, e.g., specific Ising error model and calibration of β.

c. Detailed implementation

Having seen the basic pictures of how the multipair EC works, here we write out the detailed formalism and implementation of the pictures. We start with a reminder that the multipair EC protocol attempts to identify uncorrelated errors based on the likelihood $p(\sigma_E|\sigma)$ for having errors σ_E in a given snapshot σ. In addition, using this likelihood, it estimates the number fluctuation within a domain, which is essential for computing the brane correlators. Below, we discuss how to compute $p(\sigma_E|\sigma)$ and the number fluctuation.

We first discuss how to compute $p(\sigma_E|\sigma)$. Let us assume that we get a parity snapshot σ from noisy measurement. We define σ as a set of parity flips. Some parity flips of σ are incoherent errors, and we want to remove their effect. Next, let us define the set of all possible uncorrelated error configurations that can occur in the snapshot as $S(\sigma)$. Then, the probability of σ has an error $\sigma_E \in S(\sigma)$ is given by Bayes' rule:

$$p(\sigma_E|\sigma) = \frac{\eta^{|\sigma_E|} p(\sigma - \sigma_E)}{\sum_{\sigma_i \in S(\sigma)} \eta^{|\sigma_i|} p(\sigma - \sigma_i)}, \tag{D2}$$

where η is the error probability, $|\sigma|$ is the number of parity flips of σ, and $\sigma - \sigma_E$ is the difference of the two sets σ and σ_E. Here, $p(\sigma_i)$ is the probability of getting the snapshot σ_i from a parity measurement, which is given by the square of the coefficient of the parity configuration σ_i of the underlying many-boson wave function. To compute $p(\sigma_E|\sigma)$, we need to know $p(\sigma_i)$. However, direct computation of $p(\sigma_i)$ requires simulation of the full ground state wave function, which is computationally demanding. Below, we discuss how to approximately estimate $p(\sigma_i)$, using the Ising error model as we did in the original single-pair EC protocol.

In Mott insulators, $p(\sigma_i)$ can be well approximated by the Ising error model, whose probabilities for each configuration can be obtained by the perturbative expansion of the link terms. Each link term of the Ising model (or BH model) generates a pair of parity flips. In addition, a given set of parity flips can be generated by sequentially flipping a set of parity pairs Q through perturbations, starting from the background uniform configuration which has no parity flip. For example, we consider the parity configuration Fig. 15 where four adjacent parity flips $\sigma = \{0_1, 0_2, 0_3, 0_4\}$ appear. In such configuration, the four flips $\{0_1, 0_2, 0_3, 0_4\}$ could be generated by applying three different link terms: $Q_1 = \{X_1X_2, X_3X_4\}$, $Q_2 = \{X_1X_3, X_2X_4\}$, or $Q_3 = \{X_1X_4, X_2X_3\}$. Because the initial uniform parity configuration is a product state, each weight in the lowest orders in perturbation can be approximated by a spin-spin correlator as in the single-pair case. Even more, the total weight for each Q is given by

$$W_Q = \prod_{l \in Q} \frac{1}{2} \langle X_{l_1} X_{l_2} \rangle. \tag{D3}$$

This weight will be used to compute $p(\sigma_i)$. Note that there are several ways to cover a set of parity flips with pairs of parity flips. Thus, the coefficient for a parity configuration σ is given as the sum of the weights of all the possible pairings, which gives rise to the same parity configuration σ:

$$|\psi\rangle = \sum_\sigma c_\sigma |\sigma\rangle = \sum_\sigma \left(\sum_{Q \in C(\sigma)} W_Q \right) |\sigma\rangle. \tag{D4}$$

Here, $C(\sigma)$ is the set of all possible pairings of parity flips of σ. In the above example Fig. 15, we have $C(\sigma) = \{Q_1, Q_2, Q_3\}$. In other words,

$$p(\sigma_i) = \left[\sum_{Q \in C(\sigma_i)} W_Q\right]^2. \tag{D5}$$

Next, we discuss how to estimate the number fluctuation of a domain $\mathcal{D}$ of interest. Below, we will first show that the number fluctuation is related to the mean number of boundary-crossing pairs $n_{\sigma,\partial\mathcal{D}}$ of a snapshot σ. We then discuss how to compute $n_{\sigma,\partial\mathcal{D}}$.

As we discussed in Appendix C 3, the link term $X_i X_j$ of the Ising model corresponds to the hopping term $b_i^\dagger b_j$ of the BH model. In addition, perturbation by a hopping term crossing the boundary of a domain gives unit number fluctuation in the domain. In this regard, the expectation value of the number of boundary-crossing pairs can serve as a proxy of the number fluctuation. As we noted before, for a given snapshot σ, there could be multiple true parity configurations $\sigma_0 = \sigma - \sigma_E$ (generated purely from the quantum fluctuations) with $\sigma_E \in S(\sigma)$. For each σ_0, its mean number of boundary-crossing pairs is given by

$$n_{\sigma_0,\partial\mathcal{D}} = \frac{\sum_{Q \in C(\sigma_0)} n_{Q,\partial\mathcal{D}} W_Q^2}{\sum_{Q \in C(\sigma_0)} W_Q^2}, \tag{D6}$$

where $n_{Q,\partial\mathcal{D}}$ is the number of boundary-crossing pairs of the pairing pattern Q. Finally, the mean number of boundary-crossing pairs of the snapshot σ is given by

$$n_{\sigma,\partial\mathcal{D}} = \sum_{\sigma_E \in S(\sigma)} n_{\sigma-\sigma_E,\partial\mathcal{D}} p(\sigma_E|\sigma). \tag{D7}$$

Finally, here and Fig. 5 in the main text, we calibrated β of the Ising model by fitting the pair fluctuations, instead of the brane parity correlators Appendix C 5. This change is independent of the choices on the multipair or single-pair error detection schemes. Of course, if one wishes, one can stick to the original calibration method of β by the brane parity correlators as in Appendix C 5. However, we find that the calibration via the pair fluctuation works better outside of the Mott insulator than the original EC scheme.

d. Results

We can confirm that the proposed multipair EC method improves the brane correlators further, compared to the original EC protocol. Figure 16 shows the performance of the multipair method with up to 10 local parity flips. One can see that it does not underestimate the values of brane correlators, when compared with the zero-temperature values of models with $\eta = 0$. In addition, it shows more robust performance near the critical points than the original EC.

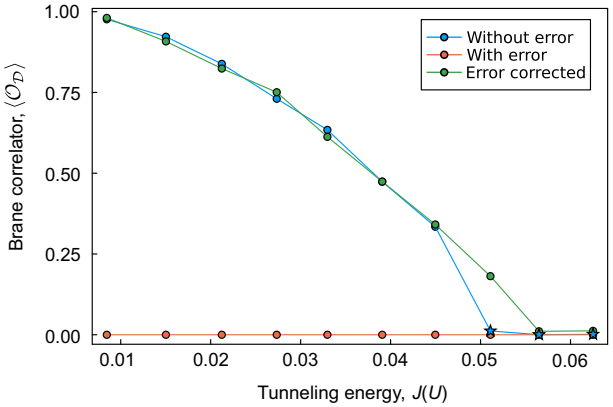

FIG. 16. Performance of multipair error-correction scheme. (a) J/U dependence of 12×12 brane correlators in a square lattice before EC (orange circles), after EC (green circles), and without errors (blue circles). The data without errors are the zero-temperature extrapolations of the brane correlators (see Appendix B) except points marked by stars which are data at $\beta = 96/U$. Parity snapshots are generated by quantum Monte Carlo simulations with the inverse temperature of $\beta = 96/U$. The chemical potential is set to be the value used to fit the experiment data.

e. Remarks

We conclude this section by making a few remarks on the improved scheme. First, this method becomes the single-pair method used in the main text by setting the maximum number of parity flips to two and performing error correction deterministically. Second, the multipair EC protocol is more computationally demanding, as the number of pairing and error patterns increases superexponentially as the number of parity flips considered in each step of the multipair EC protocol. Thus, based on the available computational resources, one needs to properly bind the number of parity flips considered at once. However, we note that this factor does not scale with the system size and thus the scalability of our original EC scheme remains the same here. Finally, as shown in the main text, even if only two parity flips are considered at once, i.e., our original single-paired EC scheme, the EC greatly improves the brane correlator compared to the uncorrected value. Thus, one could reconstruct the brane correlator extremely efficiently and effectively.

APPENDIX E: DIFFERENT LATTICE GEOMETRY

We demonstrate that our EC method can be applied to different lattice geometries such as triangular and Lieb lattices. To show this, we perform QMC simulation of BH model on the triangular and Lieb lattices and produce parity snapshots with uncorrelated error rate $\eta = 0.03$. We then conduct our EC protocol and estimate the error-corrected brane correlator. Figure 17 shows the values of brane correlator with and without the EC method. In both the

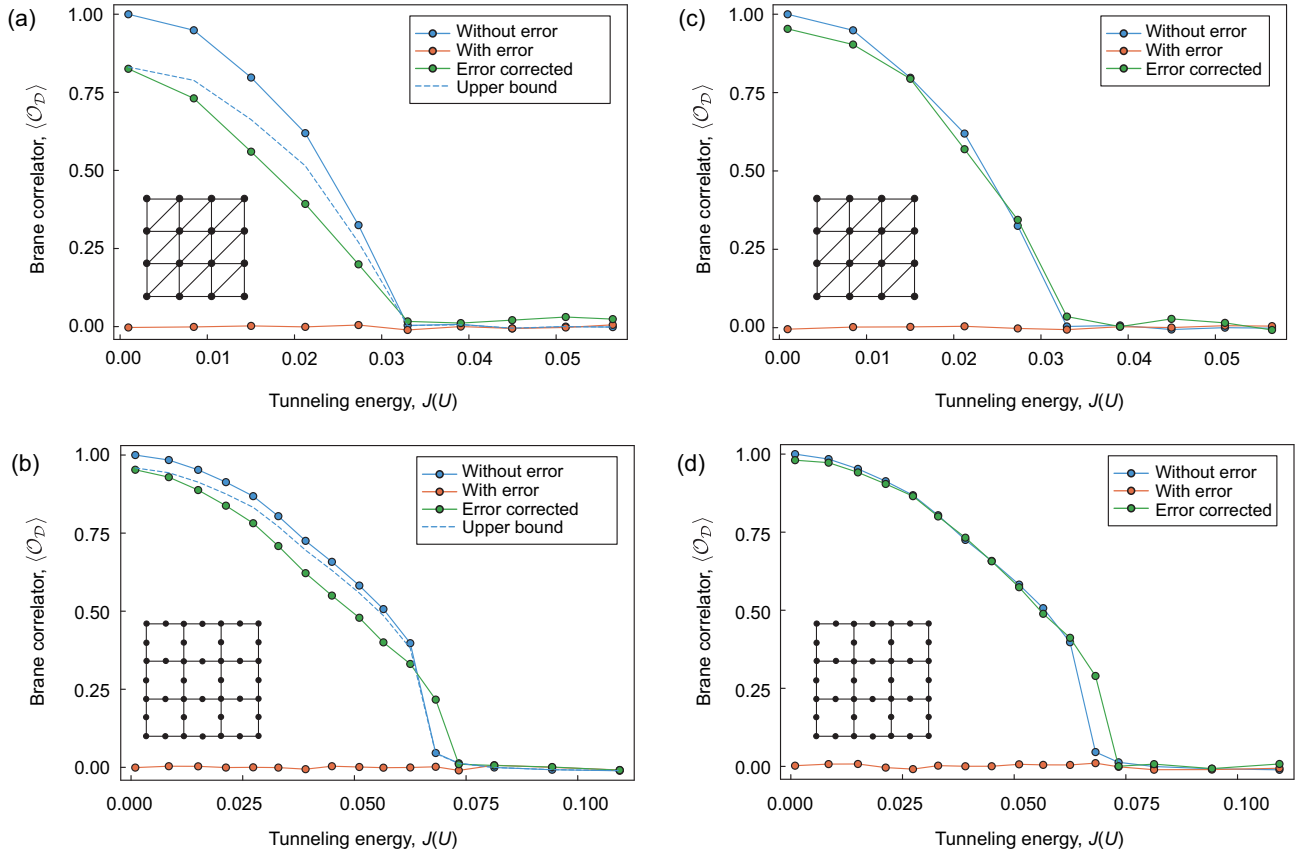

FIG. 17. Brane correlator of the Bose-Hubbard model with the error-correction method in triangular and Lieb lattices. The brane correlators $\langle \mathcal{O}_\mathcal{D} \rangle$ are evaluated on (a) a triangular lattice on the 12×12 domain and (b) a Lieb lattice with the 11×11 domain, respectively. We plot the J/U dependence of the $\langle \mathcal{O}_\mathcal{D} \rangle$ without the EC (orange circles), after single-pair EC (green circles), and without errors (blue circles). Here, we set the chemical potential $\mu = 0.6U$ in the model and the error rate $\eta = 0.03$ for the model with errors. For the model without error (blue circles), we computed the brane correlators at a fairly low temperature, namely $\beta = 96/U$. The dashed blue line indicates an upper bound of the reconstructed brane correlator for the original EC scheme, i.e., single-pair error-correction scheme. More details can be found in Appendix D 1. The critical point in the triangular lattice is at $(J/U)_c \approx 0.03$. The slight mismatch between the point where the brane correlator vanishes and the quantum critical point is attributed to the finite size of the domains. (c),(d) The brane correlators $\langle \mathcal{O}_\mathcal{D} \rangle$ in the triangular and the Lieb lattices after the improved error-correction scheme with up to 8 local parity flips (see Appendix D 2). Notably, the error-corrected values of the brane parity correlator nicely agree with the zero-temperature limit values without error.

lattices, we used both the original EC protocol (single-pair correction scheme) and improved EC protocol (multipair correction scheme). Figure 17 shows that our EC method indeed greatly improves the values of the brane correlators, which are otherwise difficult to measure.

APPENDIX F: GENERALIZED BRANE CORRELATOR

Here we will discuss the detailed definition of the statistical estimation of the generalized brane correlator, which was proposed in Ref. [15].

In this appendix, we will assume that we have already removed all uncorrelated holes via the error correction. Then, for a given parity flip at the site i, the probability that the flip is correlated with another flip at the site j is given by

$$p(i \leftrightarrow j|i) = \frac{p(i \leftrightarrow j)}{\sum_{k \neq i} p(i \leftrightarrow k)}. \tag{F1}$$

Note that it can be regarded as the mean number of particle-hole pairs connecting i and j.

For a given snapshot σ and a region $\mathcal{D}$ (embedded within $\mathcal{D}^c$), let E be the positions of parity flips. Then, the mean number of pairings $N(\mathcal{D} \to \mathcal{D}^c/\mathcal{D})$ crossing $\partial\mathcal{D}$ is

$$N(\mathcal{D} \to \mathcal{D}^c/\mathcal{D}) = \sum_{i \in E \cap \mathcal{D}, j \in \mathcal{D}^c/\mathcal{D}} p(i \leftrightarrow j|i). \tag{F2}$$

Let us consider two parity flips: $i \in \mathcal{D}$ and $j \in \mathcal{D}^c/\mathcal{D}$. Since the probability of the two flips i and j being paired is given by $p(i \leftrightarrow j|i)$, we may assign the site occupation numbers $(n_i, n_j) = (0, 2)$ or $(n_i, n_j) = (2, 0)$ (because the

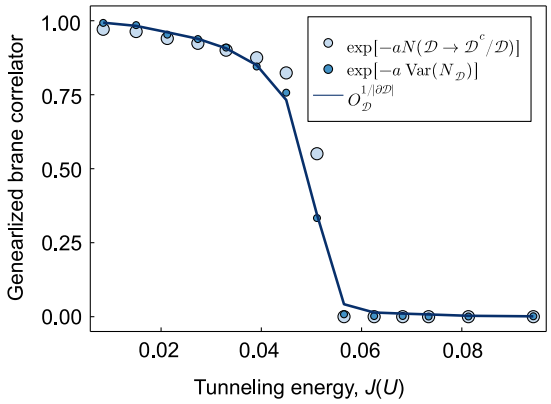

FIG. 18. Tunneling energy (J/U) dependence of the generalized brane correlator computed by three different ways: explicit computation of $O_{\mathcal{D}}^{1/|\partial\mathcal{D}|}$ in Eq. (F4), computation via the number fluctuation $\exp[-a\mathrm{Var}(N_{\mathcal{D}})]$ in Eq. (F5), and computation via the reconstructed number fluctuation $\exp[-aN(\mathcal{D}\to\mathcal{D}^c/\mathcal{D})]$ in Eq. (F6). Here, $\mathcal{D}$ is 32×32 square region, and a is the constant of $\pi^2/2|\partial\mathcal{D}|$.

mean occupation number is $\bar{n}=1$ in the MI) with the probability of $p(i\leftrightarrow j|i)/2$. The number fluctuation due to this assignment is given by $\mathrm{Var}(N)=\mathbb{E}[(n_i-1)^2]=p(i\leftrightarrow j|i)$. Here, $\mathrm{Var}(X)$ means the variance of X. Thus, the total number fluctuation in $\mathcal{D}$ is given by

$$\mathrm{Var}(N_{\mathcal{D}})=N(\mathcal{D}\to\mathcal{D}^c/\mathcal{D}), \tag{F3}$$

with $N_{\mathcal{D}}=\sum_{i\in\mathcal{D}}n_i$.

We then consider the generalized brane correlator of BH model defined on a region $\mathcal{D}$ [15]:

$$O_{\mathcal{D}}^{1/|\partial\mathcal{D}|}=e^{(i\pi/\sqrt{|\partial\mathcal{D}|})\sum_{i\in\mathcal{D}}n_i}. \tag{F4}$$

Here, $|\partial\mathcal{D}|$ is the length of a side of the square region $\mathcal{D}$. Within the Gaussian approximation, the expectation value of the generalized brane correlator is given by

$$\langle O_{\mathcal{D}}^{1/|\partial\mathcal{D}|}\rangle\approx e^{(-\pi^2/2|\partial\mathcal{D}|)\mathrm{Var}(N_{\mathcal{D}})}. \tag{F5}$$

Note that the number fluctuation $\mathrm{Var}(N_{\mathcal{D}})$ can be statistically approximated by $N(\mathcal{D}\to\mathcal{D}^c/\mathcal{D})$. Thus, we define an expression for statistical evaluation of the generalized brane correlator [15]:

$$\langle O_{\mathrm{pair},\mathcal{D}}^{1/|\partial\mathcal{D}|}\rangle=e^{(-\pi^2/2|\partial\mathcal{D}|)N(\mathcal{D}\to\mathcal{D}^c/\mathcal{D})}. \tag{F6}$$

We numerically find $\langle O_{\mathrm{pair},\mathcal{D}}^{1/|\partial\mathcal{D}|}\rangle\approx\langle O_{\mathcal{D}}^{1/|\partial\mathcal{D}|}\rangle$; see Fig. 18. Furthermore, this statistically evaluated generalized brane correlator inherits nice properties of the original proposal [15], such as negligible scaling on the domain size.

1. Proof of constant $\langle O_{\mathbf{pair},\mathcal{D}}^{1/|\partial\mathcal{D}|}\rangle$ in the MI phase

Here, we show that $\langle O_{\mathrm{pair},\mathcal{D}}^{1/|\partial\mathcal{D}|}\rangle$ remains constant in the MI phase even if we increase $|\partial D|$. We assume that all uncorrelated errors are removed already so that all the remaining flips are correlated.

Let the probability of having one of the paired parity flips be $\varepsilon/2$. It means that if we find a parity flip with the probability of $\varepsilon/2$, then there must be another flip correlated with the one we found. In the MI phase of BH model, or interchangeably the paramagnetic phase of the TFIM, the off-diagonal two-point correlator decays exponentially, i.e., $\langle X_iX_j\rangle\sim e^{-|i-j|/\xi}$ for some small ξ. We then try to compute the total number of pairings, which is the denominator of Eq. (F2). We assume that we pick a parity flip at i. Then, its pair will be at another site j with the probability proportional to $e^{-|i-j|/\xi}$. Since it is exponentially decaying, we may neglect its tail and assume that its partner is inside the ξ neighborhood of the parity flip at i.

Now, we consider other possible parings: pairings with other correlated parity flips. The probability of having another pair of errors at the distance l is $(2\pi l)\times(\varepsilon/2)$. Then, the total weight due to other pairs would be

$$\sum_{l=0}^{\infty}e^{-l/\xi}\times(2\pi l)\times(\varepsilon/2)\times 2\approx 2\pi\varepsilon e^{-l/\xi}. \tag{F7}$$

Thus, the total weight is $(1+2\pi\varepsilon)e^{-1/\xi}$. Then, let us assume that we pick a parity flip near $(<\xi)$ $\partial\mathcal{D}$ inside of $\mathcal{D}$ and the probability of the other parity flip being outside of $\mathcal{D}$ is p_{cross}. If the parity flip is adjacent to the boundary, then $p_{\mathrm{cross}}\sim 1/4$. It decays exponentially $(e^{-l/\xi})$ as the parity flip becomes farther away. We may neglect contributions from them. Then, the mean number of parings crossing the boundary is

$$N(\mathcal{D}\to\mathcal{D}^c/\mathcal{D})=\frac{\varepsilon|\partial\mathcal{D}|}{4(1+2\pi\varepsilon)e^{-1/\xi}}, \tag{F8}$$

which is vanishing for small ε.

2. Proof of vanishing $\langle O_{\mathbf{pair},\mathcal{D}}^{1/|\partial\mathcal{D}|}\rangle$ in the SF phase

Let us assume that $|\mathcal{D}^c/\mathcal{D}|\gg|\mathcal{D}|$. In addition, let us also assume that $\langle X_iX_j\rangle\sim m^2+(1-m^2)e^{-|i-j|/\xi}$ for some small ξ. Since the correlation between parity flips remains a finite constant for large $|i-j|$, one can expect that the probability of a parity flip $\mathcal{D}$ being paired with another parity flip in $\mathcal{D}^c/\mathcal{D}$ converges to unity as $|\mathcal{D}^c/\mathcal{D}|$ increases. Thus, $N(\mathcal{D}\to\mathcal{D}^c/\mathcal{D})$ converges to the number of parity flips in $\mathcal{D}$, meaning that it is proportional to $|\mathcal{D}|$. Note that since the probability of having a parity flip on a site is $1/2-\varepsilon$ for small ε, we have $N(\mathcal{D}\to\mathcal{D}^c/\mathcal{D})=|\mathcal{D}/2|$ approximately.

3. Numerical demonstration

Here, we numerically show that the generalized brane correlator can indeed be well captured by the reconstructed number fluctuation $N(\mathcal{D} \to \mathcal{D}^c/\mathcal{D})$ [Eq. (F2)]. As a demonstration, we consider the BH model on 64×64 square lattice under the periodic boundary condition with the sufficiently low temperature $(1/T = 32U)$. We collect number snapshots from QMC simulations, and using the snapshots, we compute the generalized brane correlator [Eq. (F4)]. More precisely, we compute it in three different ways: (1) direct computation from number snapshots, (2) approximated computation from the number fluctuation [Eq. (F5)], and (3) approximated computation from the reconstructed number fluctuation [Eq. (F6)]. Figure 18 compares expectation values of the generalized brane correlator with $\mathcal{D} = 32 \times 32$ computed from the three different ways. The total system size is $\mathcal{D}^c = 64 \times 64$. One can see that the Gaussian approximated generalized brane correlator agrees with the directly computed generalized brane correlator for all J/U. In addition, the generalized brane correlator computed from $N(\mathcal{D} \to \mathcal{D}^c/\mathcal{D})$ also agrees well with the values computed from QMC simulation.

[1] K. G. Wilson, *Confinement of quarks*, Phys. Rev. D **10**, 2445 (1974).

[2] M. den Nijs and K. Rommelse, *Preroughening transitions in crystal surfaces and valence-bond phases in quantum spin chains*, Phys. Rev. B **40**, 4709 (1989).

[3] T. Kennedy and H. Tasaki, *Hidden $Z_2 \times Z_2$ symmetry breaking in Haldane-gap antiferromagnets*, Phys. Rev. B **45**, 304 (1992).

[4] A. Kitaev, *Fault-tolerant quantum computation by anyons*, Ann. Phys. (Amsterdam) **303**, 2 (2003).

[5] M. B. Hastings and X.-G. Wen, *Quasiadiabatic continuation of quantum states: The stability of topological ground-state degeneracy and emergent gauge invariance*, Phys. Rev. B **72**, 045141 (2005).

[6] F. D. M. Haldane, *Nonlinear field theory of large-spin Heisenberg antiferromagnets: Semiclassically quantized solitons of the one-dimensional easy-axis Néel state*, Phys. Rev. Lett. **50**, 1153 (1983).

[7] W. S. Bakr, J. I. Gillen, A. Peng, S. Fölling, and M. Greiner, *A quantum gas microscope for detecting single atoms in a Hubbard-regime optical lattice*, Nature (London) **462**, 74 (2009).

[8] J. F. Sherson, C. Weitenberg, M. Endres, M. Cheneau, I. Bloch, and S. Kuhr, *Single-atom-resolved fluorescence imaging of an atomic Mott insulator*, Nature (London) **467**, 68 (2010).

[9] E. G. Dalla Torre, E. Berg, and E. Altman, *Hidden order in 1D Bose insulators*, Phys. Rev. Lett. **97**, 260401 (2006).

[10] E. Berg, E. G. Dalla Torre, T. Giamarchi, and E. Altman, *Rise and fall of hidden string order of lattice bosons*, Phys. Rev. B **77**, 245119 (2008).

[11] M. Endres, M. Cheneau, T. Fukuhara, C. Weitenberg, P. Schauß, C. Gross, L. Mazza, M. C. Bañuls, L. Pollet, I. Bloch, and S. Kuhr, *Observation of correlated particle-hole pairs and string order in low-dimensional Mott insulators*, Science **334**, 200 (2011).

[12] T. A. Hilker, G. Salomon, F. Grusdt, A. Omran, M. Boll, E. Demler, I. Bloch, and C. Gross, *Revealing hidden antiferromagnetic correlations in doped Hubbard chains via string correlators*, Science **357**, 484 (2017).

[13] P. Sompet, S. Hirthe, D. Bourgund, T. Chalopin, J. Bibo, J. Koepsell, P. Bojović, R. Verresen, F. Pollmann, G. Salomon, C. Gross, T. A. Hilker, and I. Bloch, *Realizing the symmetry-protected Haldane phase in Fermi-Hubbard ladders*, Nature (London) **606**, 484 (2022).

[14] C. Degli Esposti Boschi, A. Montorsi, and M. Roncaglia, *Brane parity orders in the insulating state of Hubbard ladders*, Phys. Rev. B **94**, 085119 (2016).

[15] S. Fazzini, F. Becca, and A. Montorsi, *Nonlocal parity order in the two-dimensional Mott insulator*, Phys. Rev. Lett. **118**, 157602 (2017).

[16] G. Semeghini, H. Levine, A. Keesling, S. Ebadi, T. T. Wang, D. Bluvstein, R. Verresen, H. Pichler, M. Kalinowski, R. Samajdar, A. Omran, S. Sachdev, A. Vishwanath, M. Greiner, V. Vuletić, and M. D. Lukin, *Probing topological spin liquids on a programmable quantum simulator*, Science **374**, 1242 (2021).

[17] R. Verresen, M. D. Lukin, and A. Vishwanath, *Prediction of toric code topological order from Rydberg blockade*, Phys. Rev. X **11**, 031005 (2021).

[18] Z. Cai, R. Babbush, S. C. Benjamin, S. Endo, W. J. Huggins, Y. Li, J. R. McClean, and T. E. O'Brien, *Quantum error mitigation*, arXiv:2210.00921.

[19] S. Cao, P. Tang, X. Guo, X. Chen, W. Zhang, and X. Zhou, *Extraction and identification of noise patterns for ultracold atoms in an optical lattice*, Opt. Express **27**, 12710 (2019).

[20] A. Impertro, J. F. Wienand, S. Häfele, H. von Raven, S. Hubele, T. Klostermann, C. R. Cabrera, I. Bloch, and M. Aidelsburger, *An unsupervised deep learning algorithm for single-site reconstruction in quantum gas microscopes*, Commun. Phys. **6**, 166 (2023).

[21] D. Jaksch, C. Bruder, J. I. Cirac, C. W. Gardiner, and P. Zoller, *Cold bosonic atoms in optical lattices*, Phys. Rev. Lett. **81**, 3108 (1998).

[22] M. Greiner, O. Mandel, T. Esslinger, T. W. Hänsch, and I. Bloch, *Quantum phase transition from a superfluid to a Mott insulator in a gas of ultracold atoms*, Nature (London) **415**, 39 (2002).

[23] K. Kwon, K. Kim, J. Hur, S. J. Huh, and J.-y. Choi, *Site-resolved imaging of a bosonic Mott insulator of ^{7}Li atoms*, Phys. Rev. A **105**, 033323 (2022).

[24] F. Gerbier, *Boson Mott insulators at finite temperatures*, Phys. Rev. Lett. **99**, 120405 (2007).

[25] B. Capogrosso-Sansone, S. G. Söyler, N. Prokof'ev, and B. Svistunov, *Monte Carlo study of the two-dimensional Bose-Hubbard model*, Phys. Rev. A **77**, 015602 (2008).

[26] C. Castelnovo and C. Chamon, *Quantum topological phase transition at the microscopic level*, Phys. Rev. B **77**, 054433 (2008).

[27] A. W. Sandvik, *Stochastic series expansion method with operator-loop update*, Phys. Rev. B **59**, R14157 (1999).

[28] O. F. Syljuåsen and A. W. Sandvik, *Quantum Monte Carlo with directed loops*, Phys. Rev. E **66**, 046701 (2002).
[29] E. Dennis, A. Kitaev, A. Landahl, and J. Preskill, *Topological quantum memory*, J. Math. Phys. **43**, 4452 (2002).
[30] A. G. Fowler, *Minimum weight perfect matching of fault-tolerant topological quantum error correction in average $O(1)$ parallel time*, Quantum Inf. Comput. **15**, 145 (2015).
[31] G. Duclos-Cianci and D. Poulin, *Fast decoders for topological quantum codes*, Phys. Rev. Lett. **104**, 050504 (2010).
[32] S. P. Rath, W. Simeth, M. Endres, and W. Zwerger, *Nonlocal order in Mott insulators, duality and Wilson loops*, Ann. Phys. (Amsterdam) **334**, 256 (2013).
[33] P. M. Preiss, R. Ma, M. E. Tai, J. Simon, and M. Greiner, *Quantum gas microscopy with spin, atom-number, and multilayer readout*, Phys. Rev. A **91**, 041602(R) (2015).
[34] A. M. Kaufman, M. E. Tai, A. Lukin, M. Rispoli, R. Schittko, P. M. Preiss, and M. Greiner, *Quantum thermalization through entanglement in an isolated many-body system*, Science **353**, 794 (2016).
[35] J. Koepsell, S. Hirthe, D. Bourgund, P. Sompet, J. Vijayan, G. Salomon, C. Gross, and I. Bloch, *Robust bilayer charge pumping for spin- and density-resolved quantum gas microscopy*, Phys. Rev. Lett. **125**, 010403 (2020).
[36] T. Hartke, B. Oreg, N. Jia, and M. Zwierlein, *Doublon-hole correlations and fluctuation thermometry in a Fermi-Hubbard gas*, Phys. Rev. Lett. **125**, 113601 (2020).
[37] S. Greschner, L. Santos, and D. Poletti, *Exploring unconventional Hubbard models with doubly modulated lattice gases*, Phys. Rev. Lett. **113**, 183002 (2014).
[38] K. Duivenvoorden and T. Quella, *Discriminating string order parameter for topological phases of gapped $SU(N)$ spin chains*, Phys. Rev. B **86**, 235142 (2012).
[39] A. Catuneanu, E. S. Sørensen, and H.-Y. Kee, *Nonlocal string order parameter in the $S = \frac{1}{2}$ Kitaev-Heisenberg ladder*, Phys. Rev. B **99**, 195112 (2019).
[40] T. Hartke, B. Oreg, C. Turnbaugh, N. Jia, and M. Zwierlein, *Direct observation of nonlocal fermion pairing in an attractive Fermi-Hubbard gas*, Science **381**, 82 (2023).
[41] K. J. Satzinger, Y.-J. Liu, A. Smith, C. Knapp, M. Newman, C. Jones, Z. Chen, C. Quintana, X. Mi, A. Dunsworth *et al.*, *Realizing topologically ordered states on a quantum processor*, Science **374**, 1237 (2021).
[42] I. Cong, N. Maskara, M. C. Tran, H. Pichler, G. Semeghini, S. F. Yelin, S. Choi, and M. D. Lukin, *Enhancing detection of topological order by local error correction*, arXiv:2209.12428.
[43] Z.-P. Cian, M. Hafezi, and M. Barkeshli, *Extracting Wilson loop operators and fractional statistics from a single bulk ground state*, arXiv:2209.14302.
[44] J. B. Kogut, *An introduction to lattice gauge theory and spin systems*, Rev. Mod. Phys. **51**, 659 (1979).
[45] D. Wei, D. Adler, K. Srakaew, S. Agrawal, P. Weckesser, I. Bloch, and J. Zeiher, *Observation of brane parity order in programmable optical lattices*, Phys. Rev. X **13**, 021042 (2023).
[46] T. Stöferle, H. Moritz, C. Schori, M. Köhl, and T. Esslinger, *Transition from a strongly interacting 1D superfluid to a Mott insulator*, Phys. Rev. Lett. **92**, 130403 (2004).
[47] O. F. Syljuåsen, *Directed loop updates for quantum lattice models*, Phys. Rev. E **67**, 046701 (2003).
[48] N. Prokof'ev and B. Svistunov, *Worm algorithms for classical statistical models*, Phys. Rev. Lett. **87**, 160601 (2001).